NTNU – Trondheim
Norwegian University of
Science and Technology

Assessment of Uncertainties in Estimated Wellhead Fatigue

John Marius Hegseth

Marine Technology
Submission date: June 2014
Supervisor: Carl Martin Larsen, IMT

Norwegian University of Science and Technology
Department of Marine Technology

NTNU Trondheim
Norwegian university of science and technology
Department of marinetechnology

MASTER THESIS SPRING 2014

for

Stud.tech. JOHN MARIUS HEGSETH

ASSESSMENT OF UNCERTAINTIES IN ESTIMATED WELLHAD FATIGUE

(Vurdering av usikkerheter i estimert brønnhodeutmatting)

Fatigue life of wellheads for offshore drilling has been a hot topic for the industry during the last years. A large number of design and operation parameters have influence on fatigue accumulation, and integrity of the wellhead is essential to avoid catastrophic events like the Deepwater Horizon blow-out. But the wellhead is also a very expensive unit. This means that the industry wants to have reliable methods for calculation of fatigue damage, and thereby establish rational inspection procedures and lifetime estimates.

Det Norske Veritas has recently published a proposal for a general method for calculation of fatigue damage of wellheads. There are however great uncertainties associated with the estimated fatigue damage, and current work has indicated that the method is highly conservative. The objective of the thesis is to contribute to reduce this conservatism, by identifying important uncertainties in the analysis.

The work should be divided into tasks as follows:

1. Give an overview of methods and procedures which are applied for estimation of wellhead fatigue as described in the relevant literature. Relevant design guidelines are also to be briefly summarized.

2. Establish a global drilling riser model in Sima/Riflex, and a local wellhead system model in an appropriate finite element software.

3. Perform a fatigue damage assessment for relevant hotspots in a wellhead system, based on the numerical models.

4. Identify possible uncertainties in the analysis, investigate their effect on estimated wellhead fatigue, and suggest alternative analysis options if deemed necessary.

The work may show to be more extensive than anticipated. Some topics may therefore be left out after discussion with the supervisor without any negative influence on the grading.

The candidate should in her/his report give a personal contribution to the solution of the problem formulated in this text. All assumptions and conclusions must be supported by mathematical models and/or references to physical effects in a logical manner. The candidate should apply all available sources to find relevant literature and information on the actual problem.

The report should be well organised and give a clear presentation of the work and all conclusions. It is important that the text is well written and that tables and figures are used to sup-port the verbal presentation. The report should be complete, but still as short as possible.

The final report must contain this text, an acknowledgement, summary, main body, conclusions and suggestions for further work, symbol list, references and appendices. All figures, tables and equations must be identified by numbers. References should be given by author name and year in the text, and presented alphabetically by name in the reference list. The re-port must be submitted in two copies unless otherwise has been agreed with the supervisor.

The supervisor may require that the candidate should give a written plan that describes the progress of the work after having received this text. The plan may contain a table of content for the report and also assumed use of computer resources. From the report it should be possible to identify the work carried out by the candidate and what has been found in the available literature. It is important to give references to the original source for theories and experimental results. The report should be delivered according to instructions from the faculty, and - if needed - additional material (binder, DVD/CD/memory stick) should be delivered to the supervisor.

The work will be carried out in cooperation with MARINTEK

Contact person at MARINTEK: Andreas Amundsen

Deadline: 10 June 2014

Cm. Larsen

Carl M. Larsen
Supervisor

Preface

The work presented in this Master's thesis has been carried out at the Department of Marine Technology, Norwegian University of Science and Technology (NTNU), as part of the five-year Master of Science program in Marine Technology. It has been written during the last semester, in cooperation with MARINTEK.

I would like to thank Andreas Amundsen at MARINTEK for giving me an interesting topic, providing me with input data, and for always being available on e-mail and in person. I would also like to thank my supervisor at the Department of Marine Technology, Professor Carl Martin Larsen, for his guidance and feedback during my work. Lastly, I want to thank my friends at office A2.015 for the time we have spent together.

Trondheim, June 6, 2014

John Marius Hegseth

John Marius Hegseth

Abstract

During subsea drilling, the motions of the Mobile Offshore Drilling Unit (MODU) and riser cause cyclic bending moments on the wellhead. This may lead to fatigue failure of the component, which can have severe consequences, and there are currently no international standards on how to carry out a wellhead fatigue damage assessment. Through the Joint Industry Project (JIP) *Structural Well Integrity*, a general wellhead fatigue analysis method has recently been proposed, where the fatigue damage is estimated from a global and a local finite element analysis. There are however several uncertainties regarding the modelling of the systems, which can have significant effects on the estimated fatigue life. In this thesis, some of these uncertainties are identified, and their effect on wellhead fatigue is studied.

A short description of a typical subsea drilling system is given, and relevant theory on the topic is presented. The theory consists of an introduction to dynamic response analyses of risers and fatigue life calculations for marine structures, as well as a summary of the general wellhead fatigue analysis method described in DNV (2011a).

A global riser model is established in Sima/Riflex, which is a software developed for analysis of slender marine structures. A local wellhead system model is also established in the finite element program Abaqus, and the fatigue damage in a typical North Sea well is assessed for a one year long historical operation. The first uncertainty to be studied is the modelling of interaction between conductor and soil. This is usually done using p-y curves, which relate the lateral pressure from the soil to the displacement of the structure. The method describes how to construct p-y curves for both static and cyclic loads, where the static curves are commonly used. In this thesis, the analyses are also conducted with cyclic soil springs. Another modelling aspect with respect to soil interaction investigated in the thesis is soil damping, which is not included in the standard method.

The standard is to calculate drag force on the riser in the global analysis using the maximum projected diameter of the main tube and auxiliary lines for all wave headings, which results in maximum drag. The wave heading will vary during an operation, and the effect of using the projected diameter for a flow perpendicular to the one giving maximum drag is therefore evaluated. The fluid particle velocities and accelerations used to calculate the forces on the riser are usually found from the undisturbed incoming wave, while they in reality will be affected by disturbance from the MODU. To study this effect, diffraction from a simplified MODU geometry is calculated, and included in the global analysis. In addition, directional data on weather and MODU response is used to get an indication of how significant conservative directional assumptions are for the estimated fatigue damage, as long created waves in the most unfavourable direction usually are applied.

The results from the fatigue assessment conclude that the conductor deflections for the studied well are too small for cyclic p-y curves to have an effect on estimated fatigue life. A less stiff wellhead system could get a reduction in fatigue damage, but displacements of that order may not be realistic. The results also show that reduced drag and diffraction from the MODU have relatively little effect on fatigue damage. A reduction in drag force of 23.5 % gives an increase in total fatigue damage of 9 - 10 %. Diffracted wave kinematics result in a reduction in estimated fatigue damage of 8 % for head sea waves, while a 6 % increase in fatigue damage is observed for beam sea waves. Material soil damping is seen to have a significant effect on wellhead fatigue, as the total estimated damage is reduced with 34 - 40 %, with a reduction up to 90 % for certain sea states. There are however great uncertainties associated with the calculated damping values. The results also show that using directional data can give large reductions in estimated wellhead fatigue. The estimated fatigue life of the wellhead is found to be over three times longer for head sea compared to beam sea, and a simplified spreading of the fatigue damage around the circumference of the hotspots is seen to reduce the estimated damage by 25 % in the applied environmental conditions. It can, however, be difficult to justify non-conservative directional assumptions for future operations.

Sammendrag

Ved undervannsboring vil bevegelsene til plattformen og stigerøret forårsake dynamiske laster på brønnhodet. Dette kan føre til utmattingsbrudd i komponenten, noe som kan ha alvorlige konsekvenser, og det er per dags dato ingen internasjonale standarder for hvordan utmattingsskader p brønnhoder skal estimeres. En generell analysemetode for brønnhodeutmatting har nylig blitt foreslått gjennom industriprosjektet *Structural Well Integrity*, hvor utmattingsskaden blir beregnet fra en global og en lokal elementanalyse. Det er imidlertid flere usikkerheter tilknyttet modelleringen av systemene, noe som kan ha betydelig effekt på den beregnede utmattingslevetiden. I denne oppgaven er noen av disse usikkerhetene identifisert, og deres effekt på brønnhodeutmatting er studert.

En kort beskrivelse av et typisk boresystem er gitt, og relevant teori om emnet er presentert. Teorien består av en introduksjon til dynamiske responsanalyser av stigerør og utmattingsberegninger for marine konstruksjoner, samt en oppsummering av den generelle analysemetoden for brønnhodeutmatting beskrevet i DNV (2011a).

En global stigerørsmodell er etablert i Sima/Riflex, en programvare utviklet for analyse av slanke marine konstruksjoner. En lokal modell av brønnhodesystemet er også etablert i FEM-programmet Abaqus, og utmattingsskaden i en typisk Nordsjø-brønn for en ett år lang operasjon er estimert. Den første usikkerheten som studeres er modelleringen av interaksjon mellom conductor og jord. Dette gjøres vanligvis ved hjelp av p-y-kurver, som beskriver relasjonen mellom det laterale trykket fra jorden og forskyvningene til konstruksjonen. Metoden beskriver hvordan p-y-kurver kan konstrueres for både statiske og sykliske laster, hvor de statiske kurvene ofte benyttes i analysene. I denne oppgaven er analysene også gjennomført med sykliske jordfjærer. Et annet effekt i forbindelse med jordinteraksjon undersøkt i oppgaven er jorddempning, som ikke er inkludert i standardanalysen.

Det er vanlig å beregne dragkraft på stigerøret i den globale analysen ved å bruke maksimal projisert diameter på hovedrør og hjelperør for alle bølgeretninger, noe som resulterer i maksimal drag. Bølgeretningen inn på stigerøret vil variere under en operasjon, og effekten av å bruke den projiserte diameteren for en strøm vinkelrett på den som gir maksimal drag er derfor evaluert. Væskepartikkel-hastigheter og -akselerasjoner som brukes til å beregne krefter på stigerøret blir vanligvis funnet fra de uforstyrrede innkommende bølgene, mens de i virkeligheten vil bli påvirket av forstyrrelser fra plattformen. For å studere denne effekten er diffraksjon fra en forenklet plattform-geometri beregnet, og inkludert i den globale analysen. I tillegg blir retningsdata på vær og plattform-respons brukt til å få en indikasjon på hvor viktige konservative retningsan-

tagelser er for estimert utmattingsskade, side langkammede bølger i den mest ugunstige retningen vanligvis blir brukt.

Resultatene fra utmattingsanalysen konkluderer med at utbøyningene på conductoren for den studerte brønnen er for små til at sykliske p-y-kurver har en effekt på estimert utmattingslevetid. Et mindre stivt brønnhodesystem kan få en reduksjon i estimert utmattingsskade, men forskyvninger av denne størrelsesorden er muligens ikke realistisk. Resultatene viser også at redusert drag og diffraksjon fra plattform har relativt liten effekt på utmattingsskaden. En reduksjon i dragkraft på 23.5 % gir en økning i total utmattingsskade på 9-10 %. Diffraktert bølgekinematikk resulterer i en reduksjon i estimert utmattingsskade på 8 % for bølger rett forfra, mens en 6 % økning i utmattingsskade er observert for bølger fra siden. Hysteresedempning fra jord har en betydelig effekt på brønnhodeutmatting, og den totale estimerte skaden blir redusert med 34-40 %, med en reduksjon på opptil 90 % for enkelte sjøtilstander. Det er imidlertid store usikkerheter relatert til de beregnede dempingsverdiene. Resultatene viser også at bruk av retningsdata kan gi store reduksjoner i estimert brønnhodeutmatting. Den beregnede utmattingslevetiden til brønnhodet er funnet å være over tre ganger lengre for bølger rett forfra i forhold til bølger fra siden, og en forenklet spredning av utmattingsskaden rundt omkretsen av de kritiske punktene resulterer i en reduksjon i estimert utmattingsskade på 25 % i de observerte værforholdene. Det kan imidlertid være vanskelig å rettferdiggjøre ikke-konservative retningsantagelser for en framtidig boreoperasjon.

Contents

List of Figures

List of Tables

Nomenclature

Abbreviations

API	American Petroleum Institute
ASTM	American Society for Testing and Materials
BOP	Blowout Preventer
DFF	Design Fatigue Factor
DNV	Det Norske Veritas
FE	Finite Element
FFT	Fast Fourier Transform
ISO	International Organization for Standardization
JIP	Joint Industry Project
KC	Keulegan-Carpenter
LFJ	Lower Flex Joint
LMRP	Lower Marine Riser Package
MODU	Mobil Offshore Drilling Unit
p-y	Pressure versus displacement
RAO	Response Amplitude Operator
RF	Reduction Factor
R-O	Ramberg-Osgood
SCF	Stress Concentration Factor
SN	Stress versus cycles to failure
UFJ	Upper Flex Joint
VIV	Vortex-Induced Vibrations
WAFO	Wave Analysis for Fatigue and Oceanography
JONSWAP	JOint North Sea WAve Project

Greek Symbols

α	R-O model parameter
α_1	Coefficient for mass proportional Rayleigh damping
α_2	Coefficient for stiffness proportional Rayleigh damping
β	Newmark-β parameter beta
Γ	Gamma function
γ	Newmark-β parameter gamma, JONSWAP spectrum peakedness parameter, unit soil weight, shear strain
ΔS	Stress range

ϵ	Phase angle, spectral width parameter
ε	Strain
ζ	Wave elevation
η	Diffracted wave elevation
λ	Damping ratio
ν	Poisson's ratio
ρ	Density
σ	Normal stress
τ	Shear stress
$\boldsymbol{\phi}$	Eigenvector
ω	Angular frequency

Roman Symbols

A	Cross-sectional area, wave component amplitude
$\mathbf{a}$	Connectivity matrix
a	Water particle acceleration
$\mathbf{C}$	Damping matrix
$C1$	R-O model parameter
C_D	Drag coefficient
C_M	Inertia coefficient
c	Damping coefficient, undrained shear strength
$\log C$	Intercept of SN curve with log N axis
D	Accumulated fatigue damage
D_b	Buoyancy diameter
D_h	Hydrodynamic diameter
$\mathrm{d}F$	Force per unit length
E	Young's modulus
$E[X]$	Expected value of X
F_D	Drag force
F_d	Damping force
G	Shear modulus
g	Acceleration of gravity
H_s	Significant wave height
h	Weibull distribution shape parameter
I	Second moment of area, irregularity factor
$\mathbf{K}$	Stiffness matrix
$\mathbf{k_E}$	Element elastic stiffness matrix
$\mathbf{k_G}$	Element geometric stiffness matrix
k	Stiffness coefficient, thickness exponent
l	Element length
$\mathbf{M}$	Mass matrix
m	Mass per unit length, negative inverse slope of SN curve
m_n	n^{th} moment of the energy spectrum
$\mathbf{N}$	Interpolation function
N	Cycles to failure

n	Number of load cycles
P	Element axial force
p	Fluid pressure, lateral soil resistance
$\mathbf{Q}$	Load vector
R	R-O model parameter
$R(\tau)$	Autocorrelation function
$S(\omega)$	Energy spectrum
$\mathbf{T}_j$	Transformation matrix for element j
T	Effective riser tension
T_p	Spectral peak period, force from axial stress in pipe wall
t	Plate thickness
U	Maximum strain energy stored during a load cycle
$\mathbf{u}$	Displacements at arbitrary point in element
u	Water particle velocity
u_c	Current velocity
$\mathbf{v}$, $\dot{\mathbf{v}}$, $\ddot{\mathbf{v}}$	Displacement, velocity, and acceleration vector
W_d	Energy dissipation per load cycle
w	Effective weight per unit length
w_p	Weight of empty pipe per unit length, spectral peak frequency
$\dot{x}$, $\ddot{x}$	Structural velocity and acceleration
y	Lateral pile deflection

1 Introduction

1.1 Background

Subsea drilling is often done from a Mobile Offshore Drilling Unit (MODU). The MODU is connected to the wellhead system through a drilling riser, and the motions of the MODU and the riser in current and waves impose dynamic loads on the wellhead, as shown in Figure 1.1. The dynamic loads may lead to crack growth and ultimately structural failure of the component, which can have severe consequences. It is therefore important that the methods used to estimate the fatigue life of the wellhead are reliable. The calculations are influenced by a large number of parameters, and there are currently no international standards or guidelines on how to perform a wellhead fatigue analysis. Through the Joint Industry Project (JIP) *Structural Well Integrity*, a general method for wellhead fatigue analysis has recently been proposed (DNV, 2011a). However, current work such as Russo et al. (2012), has shown that the analytical fatigue approach is highly conservative. In order to reduce the conservatism, it is essential to identify important uncertainties in the method.

A wellhead system is structurally complex, with several interacting components which can be challenging to model correctly. The system also interacts with the surrounding soil, which results in nonlinear boundary conditions dependent on depth, location, and modelling technique. A large share of wellhead systems are also installed on a template, which imposes additional interactions which need to be considered in the analysis. The analysis will also be affected by varying parameters such as casing down weight and cement level, which can be difficult to confirm for a specific well. The dynamic loads working on the wellhead are dependent on the hydrodynamic properties of the MODU and riser, as well as environmental conditions during the operation. A wellhead fatigue analysis is therefore also multidisciplinary, as knowledge within structural analysis, hydrodynamics, geotechnics and metocean is necessary when performing a fatigue damage assessment of a wellhead system.

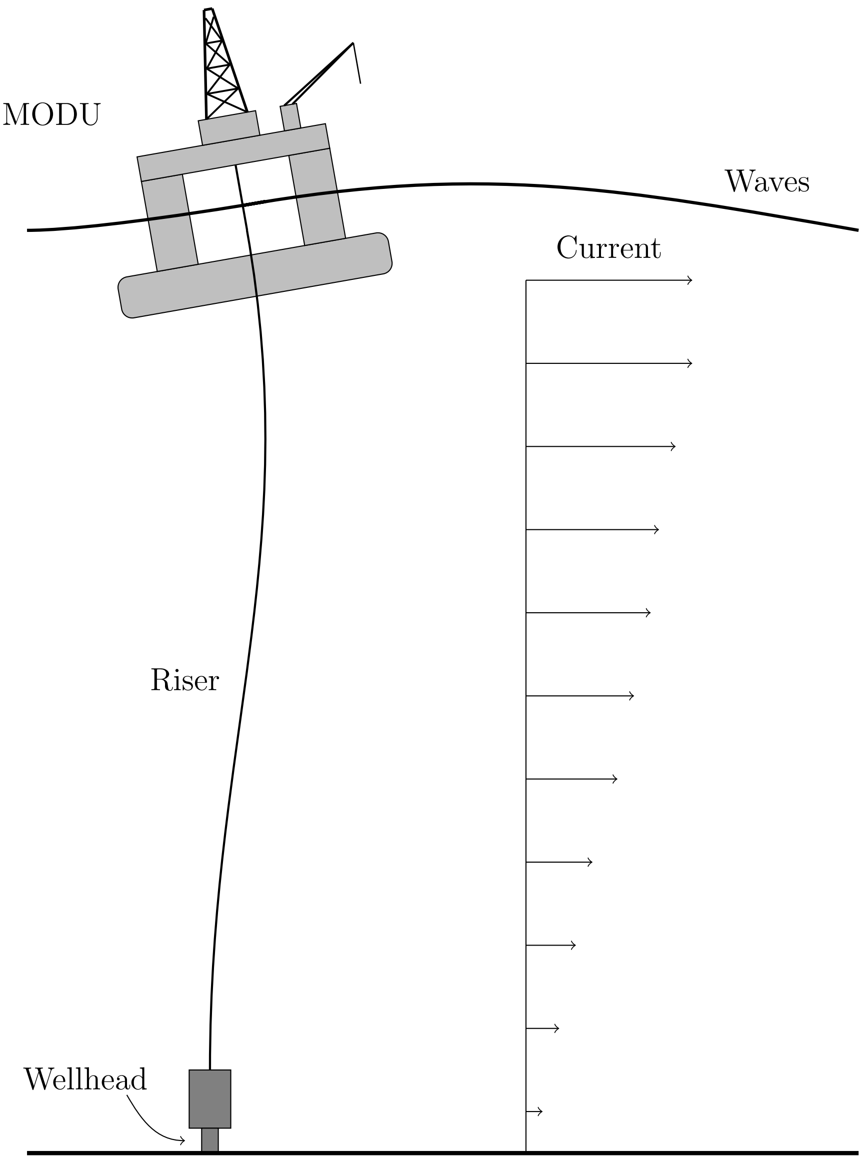

Figure 1.1: System overview.

1.2 Scope

A typical North Sea well is to be studied with respect to wellhead fatigue. An overview of methods and procedures relevant for estimation of wellhead fatigue is to be given, and the wellhead fatigue analysis method described in DNV (2011a) should be summarized. Numerical models are to be created from provided input data, and global and local analyses should be conducted using appropriate finite element (FE) software. A fatigue damage assessment is to be performed for five hotspots located on wellhead, conductor housing, conductor, and surface casing. Soil-structure interaction is to be studied, and the analyses should be performed with different representations of soil stiffness, including soil damping. Other possible sources of error in estimated wellhead fatigue originating from the global load analysis, and their effect on estimated fatigue damage, are also to be investigated.

1.3 Thesis Structure

1 Introduction
An introduction to the topic, an explanation of the scope of the thesis, and its structure.

2 System Description
An overview of the different parts of a typical marine drilling riser system, and a brief explanation of their purpose.

3 Dynamic Analysis of Risers
A short introduction to theory for solving dynamic response problems for marine risers.

4 Fatigue Theory
An introduction to how fatigue damage in a marine structure is estimated.

5 Soil Interaction
An explanation of how interaction between soil and a marine structure is modelled, and how to estimate soil damping.

6 Wellhead Fatigue Analysis Method
A brief summary of the wellhead fatigue analysis method used in this thesis.

7 Model and Analysis
An overview of the models used and analyses performed in the thesis.

8 Results and Discussion
A presentation of the results from the analyses, followed by a discussion of them.

9 Conclusions
A summary of the results, and a presentation of the conclusions drawn from them.

10 Recommendations for Further Work
Suggestions on aspects that could be investigated in future studies.

2 System Description

2.1 Drilling

In this chapter, a typical marine drilling riser system is briefly described, in order to give an overview of the different components and their functions. Subsea drilling is done in stages, where steel casings with decreasing diameter are lowered into the well and cemented in place, as illustrated in Figure 2.1.

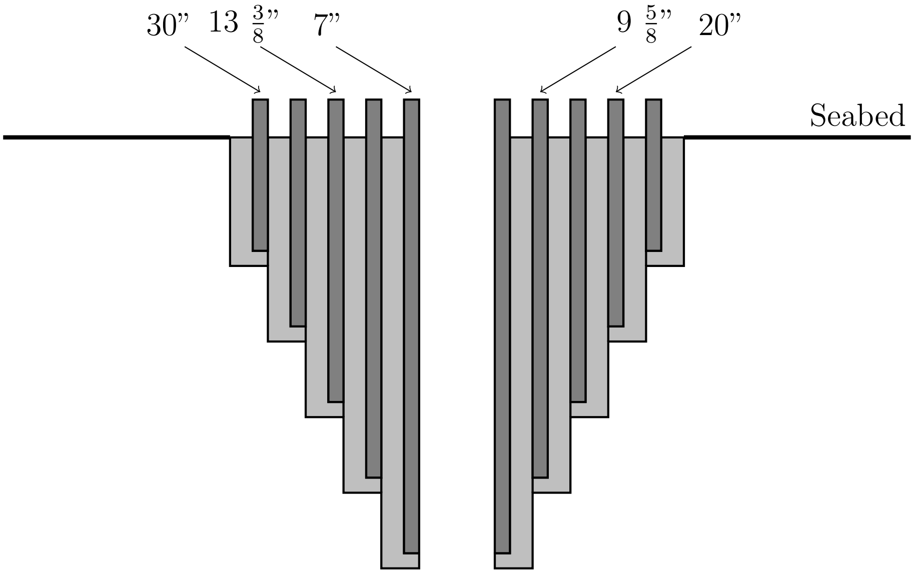

Figure 2.1: Typical casing configuration.

First, a guide base is installed on the sea bed. Then a 36" hole is drilled, and the 30" conductor is cemented in place. The holes for the conductor and the 20" surface casing are drilled without a riser, and the drill cuttings are displaced on the sea bed. After the 20" casing is installed, the BOP and riser are connected to the wellhead, and the rest of the drilling operation is done through the riser. There are three fundamental phases during a drilling operation, listed below (DNV, 2011a):

- Drilling
- Completion
- Workover

The structure of a typical marine drilling riser is shown in Figure 2.2.

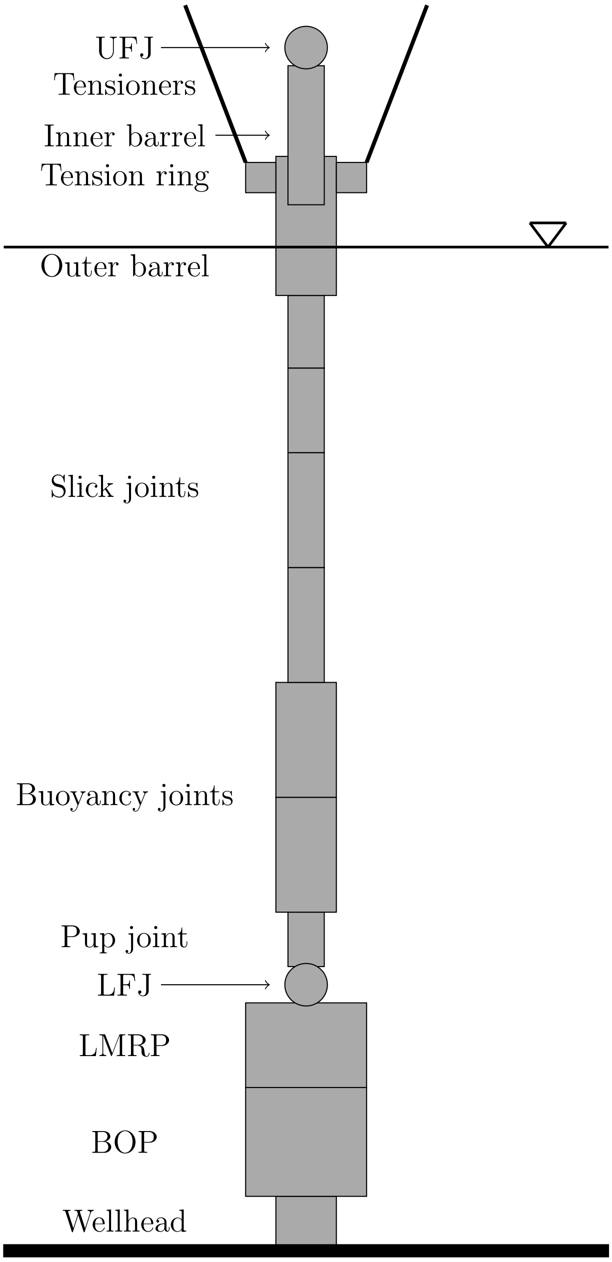

Figure 2.2: Marine drilling riser model.

2.2 Top Assembly

2.2.1 Tensioning System

Tension is applied at the top of the riser, to prevent it from buckling under its own weight. The riser tensioning system is designed to maintain a nearly constant tension force on the riser, independent of the vertical motion of the MODU. The force is applied through hydraulic tensioners, which has one end attached to the vessel, and the other end attached to the outer barrel through the tension ring (ISO, 2009).

2.2.2 Slip Joint

The slip joint consists of the inner and outer barrel. The former is connected to the vessel, while the latter is connected to the riser and tension ring. The purpose of the slip joint is to allow vertical motion of the MODU, which is done by sliding the inner barrel in and out of the outer barrel.

2.2.3 Drilling Mud

During the drilling operation, mud passes down the drill pipe, exits at the drill bit, and returns through the riser. The purpose of the drilling mud, which usually consists of bentonite and barite dissolved in water or oil, is to lubricate the drill bit, remove drill cuttings, and keep formation fluids from entering the well bore (Mather, 1995).

2.3 Riser

2.3.1 Slick/pup Joints

Slick joints are regular riser joints of different length, and the main components in the riser system. They consists of pipes in high-strength steel, which contain the drill string and return fluid from the well (ISO, 2009). Pup joints are slick joints of non-standard length, which are used to reach the exact required length.

2.3.2 Buoyancy Joints

To reduce the required top tension, and get a more evenly distributed effective tension, buoyancy modules can be attached to the riser joints. The buoyancy modules are often made of a light composite material, which causes the total joint to get a reduced submerged weight.

2.3.3 Flex Joints

Flex joints are usually connected to the riser at both ends. The purpose of the flex joints is to allow rotations of the riser, thereby reducing the transferred bending moments (ISO, 2009). The two flex joints are commonly called the upper flex joint (UFJ) and the lower flex joint (LFJ).

2.3.4 Choke/kill and Booster Lines

Choke/kill and booster lines are lines which run along the outside of the riser from the lower stack to the surface. The purpose of the choke/kill lines is to provide a controlled flow of oil, gas or drilling mud from the well bore when the blowout preventer has sealed off the well (ISO, 2009). The booster line injects drilling mud into the riser just above the lower stack, to increase the upwards flow of drill cuttings.

2.4 Lower Stack

2.4.1 Blowout Preventer (BOP)

When the drill bit encounters formations containing hydrocarbons, the pressure in the formation may be greater than the hydrostatic pressure from the drilling mud, which leads to fluids from the formation entering the well bore. This situation is called a kick, and must be controlled before it escalates into a blowout (Mather, 1995). The BOP seals off the well and controls the pressure, which can be done in several ways (see Figure 2.3) (Mather, 1995):

- Pipe rams are designed to seal around the drill pipe.
- Blind rams seal the well bore completely in the absence of a drill pipe.
- Blind/shear rams are used when it may be necessary to disconnect the rig from the well rapidly because of the weather conditions. The edges are capable of cutting the drill string and sealing the well bore under high pressure.

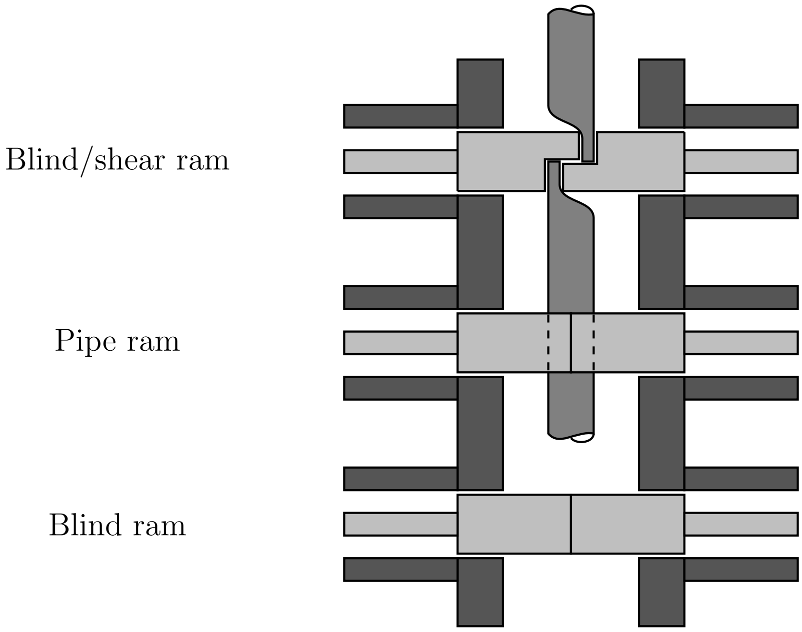

Figure 2.3: BOP with different rams.

2.4.2 Lower Marine Riser Package (LMRP)

The LMRP is the connection between the BOP and the riser, and contains a riser adapter, control pods, and the LFJ. In an emergency situation, it may be necessary to disconnect the LMRP from the BOP. It is therefore important that the lower end of the LMRP has a positive net tension (Stange, 2012).

2.4.3 Wellhead

The wellhead is located on the sea bed, where its main purposes are to support the BOP, and seal off the well during drilling (Sheffield, 1980). During cementing, the casing is hung off by a casing hanger in the wellhead, which then takes the full weight of the casing. A simplified wellhead system is shown in Figure 2.4.

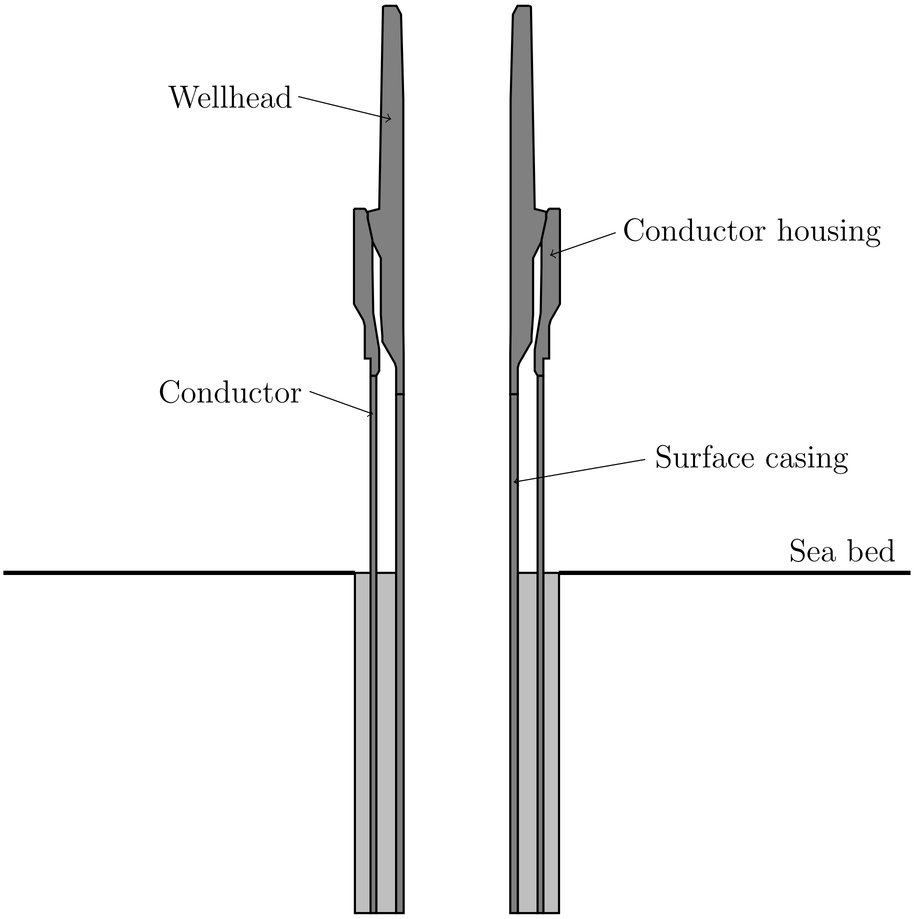

Figure 2.4: Wellhead system.

3 Dynamic Analysis of Risers

3.1 Finite Element Model

The equilibrium equation which needs to be solved in dynamic analysis is written:

$$\mathbf{M}\ddot{\mathbf{v}} + \mathbf{C}\dot{\mathbf{v}} + \mathbf{K}\mathbf{v} = \mathbf{Q}(t) \tag{3.1}$$

where:

$\mathbf{M}$	Mass matrix
$\mathbf{C}$	Damping matrix
$\mathbf{K}$	Stiffness matrix
$\mathbf{Q}$	External load vector
$\mathbf{v}$	Displacement vector
$\dot{\mathbf{v}}$	Velocity vector
$\ddot{\mathbf{v}}$	Acceleration vector

Risers are normally modelled using beam elements, and the matrices can therefore be found using the corresponding finite element formulation. A linear 2D beam element is illustrated in Figure 3.1.

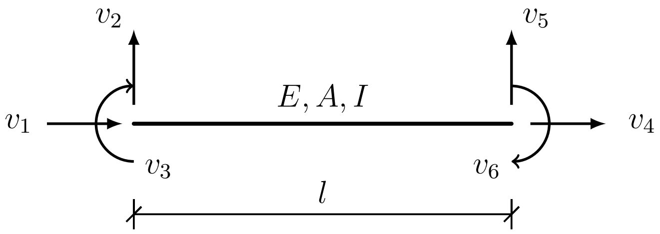

Figure 3.1: 2D linear beam element.

The mass matrix contains both structural and hydrodynamic mass, and can either be lumped or consistent. The consistent mass matrix is found from

$$\mathbf{M} = m \int_l \mathbf{N}^T \mathbf{N} \mathrm{d}x \tag{3.2}$$

where m is mass per unit length, and $\mathbf{N}$ is a set of interpolation functions relating displacements at an arbitrary point, $\mathbf{u}$, to the nodal displacements:

$$\mathbf{u} = \mathbf{N}\,\mathbf{v}. \tag{3.3}$$

A lumped mass matrix is sometimes preferred, as the non-diagonal terms in **M** increase the computation time. This means that the mass of the element is concentrated at the diagonal, while the coupling terms are neglected. The easiest lumping procedure is to sum each row in the mass matrix and place it on the diagonal, which means that the i^{th} diagonal term becomes (Mosalam, 2013):

$$\mathbf{M_{ii}} = m \int_l \mathbf{N}_i \mathrm{d}x. \tag{3.4}$$

A problem with the row summing procedure is that it may result in negative mass coefficients for certain elements, which is physically impossible and gives incorrect solutions for dynamic problems. An alternative summing procedure, called HRZ lumping, solves this problem by scaling the diagonal terms in the consistent mass matrix to preserve the total mass.

Fluid drag, soil, and the structure itself will contribute to the damping matrix, and the terms are often difficult to quantify (Langen and Sigbjörnsson, 1979). The most common way to include damping in the dynamic equilibrium equation is to use linear viscous damping. In this model the damping force, F_d, is proportional to and in phase with the velocity, as in Eq. (3.1). The damping ratio relative to critical damping for a spring-dashpot model in harmonic oscillations (see Figure 3.2) can be found from

$$\lambda = \frac{W_d}{4\pi U} = \frac{c\omega}{2k} \tag{3.5}$$

where W_d is the energy dissipation per cycle, given as

$$W_d = \oint F_d \, \mathrm{d}u = \pi c \omega u_0^2 \tag{3.6}$$

and U is the maximum strain energy stored during the cycle, given as

$$U = \frac{1}{2} k u_0^2. \tag{3.7}$$

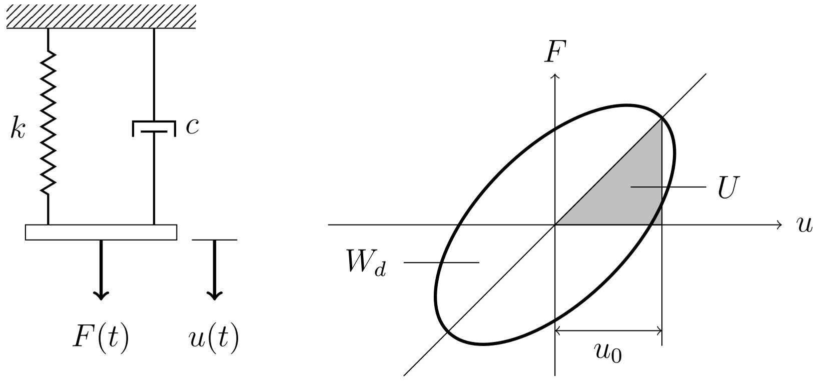

Figure 3.2: Linear viscous damping model.

If the damping is not viscous, an equivalent linear viscous damping model can be established, in order for the energy loss per cycle to be the same. The equivalent viscous damping coefficient then becomes

$$c_{eq} = \frac{W_d}{\pi \omega u_0^2} = \frac{2k\lambda}{\omega}. \tag{3.8}$$

If shear deformations are neglected, Euler-Bernoulli beam theory can be applied, and it can then be shown that the elastic stiffness matrix for the element becomes (Cook et al., 2002)

$$\mathbf{k_E} = \begin{bmatrix} \frac{EA}{l} & 0 & 0 & -\frac{EA}{l} & 0 & 0 \\ 0 & \frac{12EI}{l^3} & -\frac{6EI}{l} & 0 & -\frac{12EI}{l^3} & -\frac{6EI}{l^2} \\ 0 & -\frac{6EI}{l^2} & \frac{4EI}{l} & 0 & \frac{6EI}{l^2} & \frac{2EI}{l} \\ -\frac{EA}{l} & 0 & 0 & \frac{EA}{l} & 0 & 0 \\ 0 & -\frac{12EI}{l^3} & \frac{6EI}{l^2} & 0 & \frac{12EI}{l^3} & \frac{6EI}{l^2} \\ 0 & -\frac{6EI}{l^2} & \frac{2EI}{l} & 0 & \frac{6EI}{l^2} & \frac{4EI}{l} \end{bmatrix} \tag{3.9}$$

There will also be a contribution from geometric stiffness in the global stiffness matrix, which can be found by including second order strains:

$$\varepsilon(x, y) = \frac{\partial v_x}{\partial x} - y\frac{\partial^2 v_y}{\partial x^2} + \frac{1}{2}\left(\frac{\partial v_y}{\partial x}\right)^2. \tag{3.10}$$

The geometric stiffness matrix includes both the rope effect, shown in Figure 3.3, and effects due to beam curvature (Larsen, 1990). If the terms are linearised, the geometric stiffness matrix can be written

$$\mathbf{k_G} = \begin{bmatrix} 0 & 0 & 0 & 0 & 0 & 0 \\ 0 & \frac{6P}{5l} & -\frac{P}{10} & 0 & -\frac{6P}{5l} & -\frac{P}{10} \\ 0 & -\frac{P}{10} & \frac{2Pl}{15} & 0 & \frac{P}{10} & -\frac{Pl}{30} \\ 0 & 0 & 0 & 0 & 0 & 0 \\ 0 & -\frac{6P}{5l} & \frac{P}{10} & 0 & \frac{6P}{5l} & \frac{P}{10} \\ 0 & -\frac{P}{10} & -\frac{Pl}{30} & 0 & \frac{P}{10} & \frac{2Pl}{15} \end{bmatrix} \tag{3.11}$$

where P is the axial force in the element. The total stiffness matrix for element j is the sum of the elastic and geometric stiffness:

$$\mathbf{k}_j = \mathbf{k}_{\mathbf{E}j} + \mathbf{k}_{\mathbf{G}j} \tag{3.12}$$

and the system stiffness matrix becomes (Larsen, 1990)

$$\mathbf{K} = \sum_j \mathbf{a}_j^{\mathrm{T}} \mathbf{T}_j \mathbf{k}_j \mathbf{T}_j^{\mathrm{T}} \mathbf{a}_j \tag{3.13}$$

where $\mathbf{a}$ is the connectivity matrix, relating local and global degrees of freedom, and $\mathbf{T}_j$ is the transformation matrix for element j, which transforms the element stiffness matrices to global coordinates.

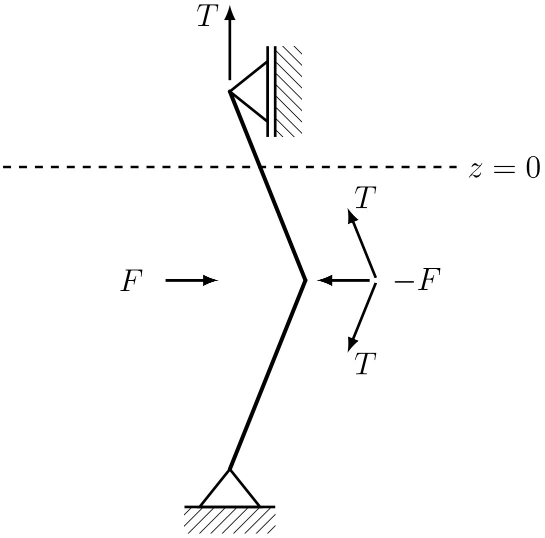

Figure 3.3: Resisting forces due to change in geometry.

For a general three-dimensional case, the riser is modelled using beam elements with 12 degrees of freedom, as shown in Figure 3.4. The following assumptions then forms the basis for the applied beam theory (MARINTEK, 2013*a*):

- Plane sections normal to the secant between the nodes remain plane and normal when deformed.
- Small strains.
- Lateral contraction because of axial elongation is neglected.
- St. Venant torsion is accounted for, while shear deformations are neglected.
- Coupling effects between torsion and bending are neglected.

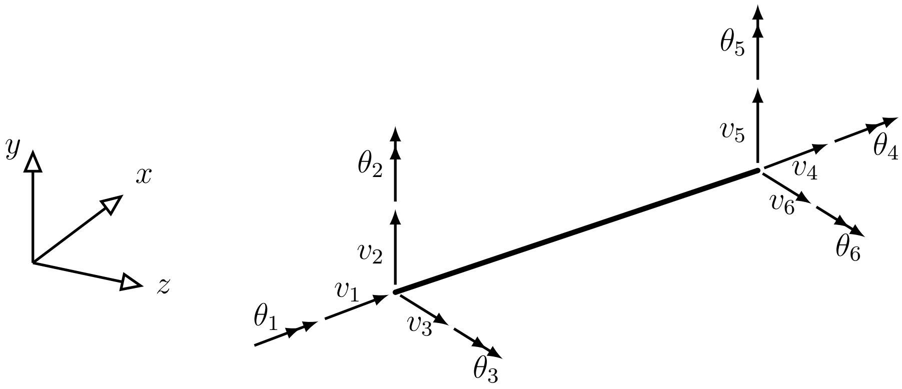

Figure 3.4: General 3D beam element.

3.2 Effective Tension

In static and dynamic analysis of marine risers, which is submerged in water and where the inside may be filled with drilling mud, it is convenient to consider equilibrium in terms of effective tension and effective weight (Sparks, 1984):

$$T = T_p - A_i p_i + A_e p_e \tag{3.14}$$

$$w = w_p + A_i \rho_i g - A_e \rho g \tag{3.15}$$

where

T	Effective tension
T_p	Resulting force from axial stresses in pipe wall
A_i	Internal cross section area
A_e	External cross section area
p_i	Internal pressure
p_e	External pressure
w	Effective weight per unit length
w_p	Weight of empty pipe per unit length
ρ_i	Density of internal fluid
ρ	Water density
g	Acceleration of gravity

The advantage of using this concept is that the pressure effects can be represented by conservative forces working in the vertical direction. The effective tension is also used to calculate the beam buckling load and geometric stiffness for the riser, and it does not represent any loss of accuracy (Larsen, 2008).

3.3 Eigenvalue Analysis

For a free, undamped oscillation, Eq. (3.1) can be written

$$\mathbf{M}\ddot{\mathbf{v}} + \mathbf{K}\mathbf{v} = 0. \tag{3.16}$$

Assuming that the solution can be written on the form

$$\mathbf{v} = \boldsymbol{\phi} \sin(\omega t), \tag{3.17}$$

Eq. (3.16) can be written as an eigenvalue problem:

$$(\mathbf{K} - \omega^2 \mathbf{M})\boldsymbol{\phi} = 0. \tag{3.18}$$

The solution to the eigenvalue problem with n degrees of freedom is a set of n eigenvalues (ω_1^2, ω_2^2, ..., ω_n^2), where each eigenvalue represents an eigenfrequency, ω_i. Each eigenvalue also has a corresponding eigenvector, $\boldsymbol{\phi}_i$, which represents the shape of the mode connected to the eigenfrequency. All possible deformation states can be described as a weighted sum of the eigenvectors, and it can be shown that they are orthogonal with respect to the mass and stiffness matrix (Larsen, 1990):

$$\boldsymbol{\phi}_i \mathbf{M} \boldsymbol{\phi}_j = 0 \text{ for } i \neq j, \tag{3.19}$$

$$\boldsymbol{\phi}_i \mathbf{K} \boldsymbol{\phi}_j = 0 \text{ for } i \neq j. \tag{3.20}$$

The damping matrix is often expressed as a linear combination of **M** and **K**, called Rayleigh damping:

$$\mathbf{C} = \alpha_1 \mathbf{M} + \alpha_2 \mathbf{K}. \tag{3.21}$$

An important consequence of this is that the eigenvectors also becomes orthogonal with respect to the damping matrix. The modal damping ratio relative to critical, λ_i, can then be written as (Langen and Sigbjörnsson, 1979):

$$\lambda_i = \frac{1}{2}\left(\frac{\alpha_1}{\omega_i} + \alpha_2 \omega_i\right). \tag{3.22}$$

3.4 Hydrodynamic Loads

The hydrodynamic forces on the riser due to waves and current are found from Morison's equation, where the horizontal motion of the riser is included (DNV, 2010):

$$\mathrm{d}F = \rho\pi\frac{D_b^2}{4}C_M a - \rho\pi\frac{D_b^2}{4}(C_M - 1)\ddot{x} + \frac{\rho}{2}C_D D_h |u - \dot{x}|(u - \dot{x}) \tag{3.23}$$

where:

$\mathrm{d}F$	Force per unit length
ρ	Water density
C_M	Inertia coefficient
C_D	Drag coefficient
D_b	Buoyancy diameter
D_h	Hydrodynamic diameter
u	Water particle velocity
a	Water particle acceleration
$\dot{x}$	Structural velocity
$\ddot{x}$	Structural acceleration

The buoyancy diameter is given by

$$D_b = \sqrt{D_{riser}^2 + n_{kc} D_{kc}^2 + D_{bst}^2} \tag{3.24}$$

where n_{kc} and D_{kc} are the number of choke/kill lines and their outer diameter, respectively. D_{bst} is the outer diameter of the booster line. The hydrodynamic diameter is calculated from

$$D_h = D_{riser} + n_{kc} D_{kc}. \tag{3.25}$$

If a regular wave is applied, the inertia force and drag force at a given depth and time will be proportional to $\cos(x)$ and $\sin^2(x)$, respectively. This is illustrated in Figure 3.5.

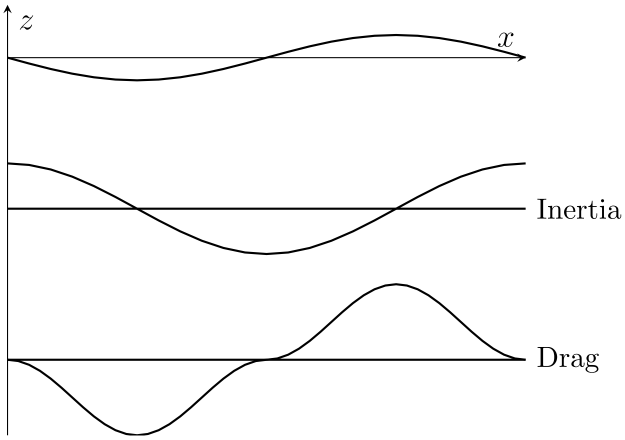

Figure 3.5: Relation between inertia and drag force for a linear wave (forces not to scale).

Current velocity is usually assumed to be constant, which means that the loads from the current are static. However, since the drag force term is quadratic, the current velocity must be included in the dynamic analysis. This can be done by subtracting the static part from the total drag force:

$$F_D^{dynamic} = F_D - F_D^{static} \tag{3.26}$$

where F_D is found from the drag term in Eq. (3.23), and F_D^{static} is the static drag force from the current, found from

$$F_D^{static} = \frac{\rho}{2} C_D D_h |u_c| u_c \tag{3.27}$$

with u_c being the current velocity (Larsen, 1990). If the dynamic equilibrium equation is solved in the time domain, the quadratic drag term can be included in the load vector directly. This is not the case for an analysis in the frequency domain, where the drag force needs to be linearised.

3.5 Stochastic Theory

A stochastic process is described by its statistical properties, since the value cannot be accurately predicted for any chosen time. If the statistical properties don't change over time, the process is said to be stationary. The wave elevation, which is a stochastic variable, is considered to be stationary within a time limit of three to six hours (Almar-Næss et al., 1985). This is used in calculations, where a sea state with constant significant wave height, H_s, and spectral peak period, T_p, usually is assumed to be three hours. Within this time limit, the waves can be represented by a spectrum, $S(\omega)$, which may be used to calculate all statistical parameters (Larsen, 1990). The spectrum for a zero mean Gaussian process, $X(t)$, is defined as

$$S(\omega) = \frac{1}{2\pi} \int_{-\infty}^{\infty} R(\tau) e^{-i\omega\tau} \mathrm{d}\tau \tag{3.28}$$

where

$$R(\tau) = E[X(t)X(t+\tau)] \tag{3.29}$$

is the autocorrelation function of the process, which correlates the wave elevation at a time instant with its past or future (Mansour and Liu, 2008). $S(\omega)$ is an even function, and since negative frequencies do not have any physical meaning, a one-sided spectrum is usually applied:

$$S^{+}(\omega) = \begin{cases} 2S(\omega), & \omega \geq 0 \\ 0, & \omega < 0. \end{cases} \tag{3.30}$$

A common spectral model is the JONSWAP spectrum (Hasselmann et al., 1973), which is expressed as

$$S^{+}(\omega) = \frac{\alpha g^2}{\omega^5} \exp\left(-1.25\left(\frac{\omega_p}{\omega}\right)^4\right) \gamma^{\exp\left(-\frac{(\omega-\omega_p)^2}{2\sigma^2\omega_p^2}\right)} \tag{3.31}$$

where γ is the peakedness parameter, and

$$\sigma = \begin{cases} 0.07, & \omega \leq \omega_p \\ 0.09, & \omega > \omega_p. \end{cases} \tag{3.32}$$

α is originally related to the mean wind speed, but for offshore applications in the North Sea, the following modified form is often used (Næss and Moan, 2013):

$$\alpha = 5.058\frac{H_s^2}{T_p^4}\left(1 - 0.287\ln\gamma\right). \tag{3.33}$$

The wave elevation time series at a given position can then be written as a sum of harmonic components (Faltinsen, 1990):

$$\zeta(t) = \sum_{j=1}^{N} A_j \sin(\omega_j t + \epsilon_j) \tag{3.34}$$

where ϵ_j is a random phase angle, and

$$\frac{1}{2}A_j^2 = S^{+}(\omega_j)\Delta\omega. \tag{3.35}$$

Another way to generate the time series is to use Fast Fourier Transform (FFT). In this method, the whole time series is generated at once by discrete Fourier transform, which is significantly faster than the method in Eq. (3.34) (Larsen, 1990).

3.6 Time Domain Analysis

When a time series of the external load is given, the dynamic equilibrium equation can be solved by numerical step-by-step integration in the time domain. The velocity and the displacement are found by integrating the acceleration twice for each time step, where the variation of the acceleration over the interval has to be assumed. There are different methods for describing this variation, as illustrated in Figure 3.6.

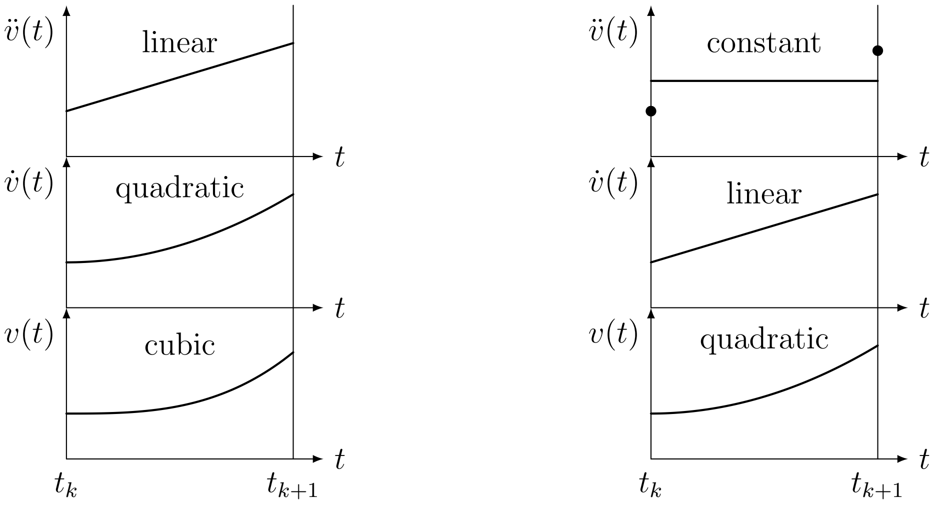

(a) Linear acceleration. **(b)** Constant average acceleration.

Figure 3.6: Two different methods for acceleration variation.

A common choice is the Newmark-β family of methods. Here, the velocity and displacement at step $k+1$ are given as

$$\dot{v}_{k+1} = \dot{v}_k + (1-\gamma)\Delta t\, \ddot{v}_k + \gamma \Delta t\, \ddot{v}_{k+1} \tag{3.36}$$

$$v_{k+1} = v_k + \Delta t\, \dot{v}_k + \left(\frac{1}{2} - \beta\right) \Delta t^2\, \ddot{v}_k + \beta \Delta t^2\, \ddot{v}_{k+1} \tag{3.37}$$

which are found from Taylor series approximation (Langen and Sigbjörnsson, 1979). The acceleration at step $(k+1)$ is then calculated from Eq. (3.1). The method is unconditionally stable if

$$\gamma \geq \frac{1}{2} \tag{3.38}$$

$$\beta \geq \frac{1}{4}\left(\gamma + \frac{1}{2}\right)^2 \tag{3.39}$$

where $\gamma = {}^1/_2$ is almost always chosen, as it ensures no artificial damping (Langen and Sigbjörnsson, 1979).

4 Fatigue Theory

4.1 Fatigue Damage Characteristics

Fatigue is caused by cyclic loads, where the stresses are too small to cause immediate failure. Instead, the structure fails after a certain number of load cycles. The most important load parameter is the stress range, i.e. the difference between the maximum and minimum stress in a load cycle. The fatigue history of a structure can be divided into three stages (Almar-Næss et al., 1985):

I Initiation

II Crack growth

III Final failure

where only stage I and II are of interest when estimating the fatigue life for a marine structure. For an un-welded component, most of the fatigue life is spent in stage I, whereas for a welded component, the majority of the fatigue life is spent in stage II (DNV, 2011a). The stress component which mainly influence fatigue damage is different for the two stages. For crack initiation, the most important stress component is the one governing yield, i.e. the von Mises stress, while the maximum principal stress is the most important component for crack growth (DNV, 2011a).

4.2 Variable Amplitude Loading

Because of varying forces from waves, currents and wind, the load cycles on a marine structure will usually not have a constant amplitude. To be able to calculate the fatigue damage under variable amplitude loading, the load history is divided into blocks. Each block contains all load cycles with a stress range $\Delta S \pm \delta S$, which are assumed to have a constant stress range of ΔS.

A description of the terminology related to variable amplitude loading is illustrated in Figure 4.1, and can be found in ASTM (2011):

- Peak is the point where the first derivative of the load history changes sign from positive to negative.
- Valley is the point where the first derivative of the load history changes sign from negative to positive.
- Reversal is the point where the first derivative of the load history changes sign.

- Range is the algebraic difference between successive peak and valley loads (-), or between successive valley and peak loads (+).
- Mean Crossing is the number of times that the load history crosses the mean-load level with a positive slope.
- Reference Load is the load under steady-state condition.

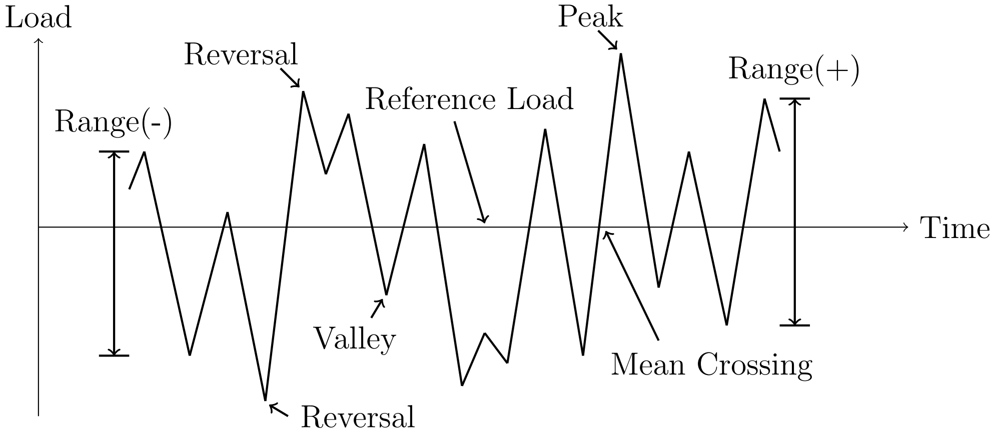

Figure 4.1: Definitions in variable amplitude loading. Adapted from ASTM (2011).

It is also common to measure the irregularity of the load history, i.e. how broad banded the signal is. This is done using the irregularity factor, which is defined as the ratio of mean crossings to the number of peaks in the load history (Almar-Næss et al., 1985):

$$I = (1 - \epsilon^2)^{0.5} \tag{4.1}$$

where the spectral width parameter, ϵ, is defined as

$$\epsilon = \left(1 - \frac{m_2^2}{m_0 m_4}\right)^{\frac{1}{2}} \tag{4.2}$$

and m_n is the n^{th} moment of the energy spectrum of the process:

$$m_n = \int_0^\infty \omega^n S(\omega) \mathrm{d}\omega. \tag{4.3}$$

4.3 SN-curves

The fatigue life of a structural component is usually expressed by an SN curve, where cycles to failure is plotted against stress range. The design SN curve is given as the mean curve minus two standard deviations for relevant experimental data, and has the following form

$$N(\Delta S)^m = C \tag{4.4}$$

where N is the number of cycles to failure, ΔS is the stress range, and C and m are constants. Using a log-log scale, the SN curve is linear, and Eq. (4.4) can be written as

$$\log N = \log C - m \log \Delta S. \tag{4.5}$$

In this equation, $\log C$ becomes the intercept with the $\log N$ axis, and m becomes the negative inverse slope of the SN curve. Experiments have shown that the fatigue life of welded joints decreases as the plate thickness increases (Almar-Næss et al., 1985). A thickness correction must therefore be applied if the plate thickness is larger than the reference thickness, and the SN curve becomes

$$\log N = \log C - m \log \left(\Delta S \left(\frac{t}{t_{ref}} \right)^k \right) \tag{4.6}$$

where t is the plate thickness, t_{ref} is the reference thickness, and k is the thickness exponent for the curve. If the plate thickness is smaller than the reference thickness, t_{ref} is used. For constant amplitude loading, the SN curve has a fatigue limit, ΔS_l, and stress ranges below this value do not contribute to fatigue damage. For variable amplitude loading, there will be cycles both above and below the fatigue limit, which will be gradually lowered as the cycles above ΔS_l will contribute to crack growth (Berge, 2006). This is often modelled using a Haibach model, where the SN curve gets a negative inverse slope of ($2m$-1) below the original fatigue limit. The result is a bilinear SN curve, as illustrated in Figure 4.2.

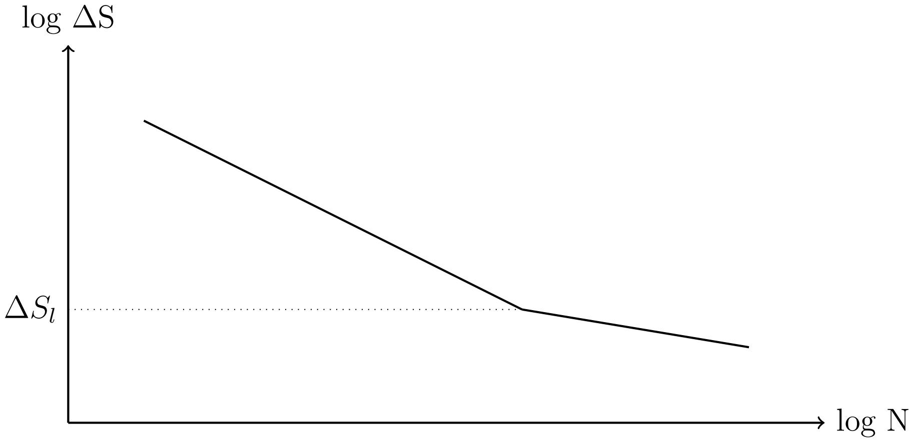

Figure 4.2: Bilinear SN curve.

The stress range used in the calculations must also take into account the local geometry. It is therefore often expressed as

$$\Delta S = SCF \cdot \Delta S_{nominal} \tag{4.7}$$

where SCF is the stress concentration factor for the analysed point, and $\Delta S_{nominal}$ is the nominal stress range (DNV, 2012a).

4.4 Cycle Counting

For variable amplitude loading, the stress history is divided into individual cycles, which are summed up in order to make a stress range histogram. However, for broad banded loading the definition of a cycle is not obvious, and the resulting cycle count will be dependent on the counting method. It is therefore important to use a procedure which gives a correct representation of the physical process of fatigue. A common choice is rainflow counting, which is compatible with the corresponding stress/strain relation (Anzai and Endo, 1979). In this method, a cycle is counted each time a hysteresis loop is closed in the stress/strain curve. This is illustrated in Figure 4.3.

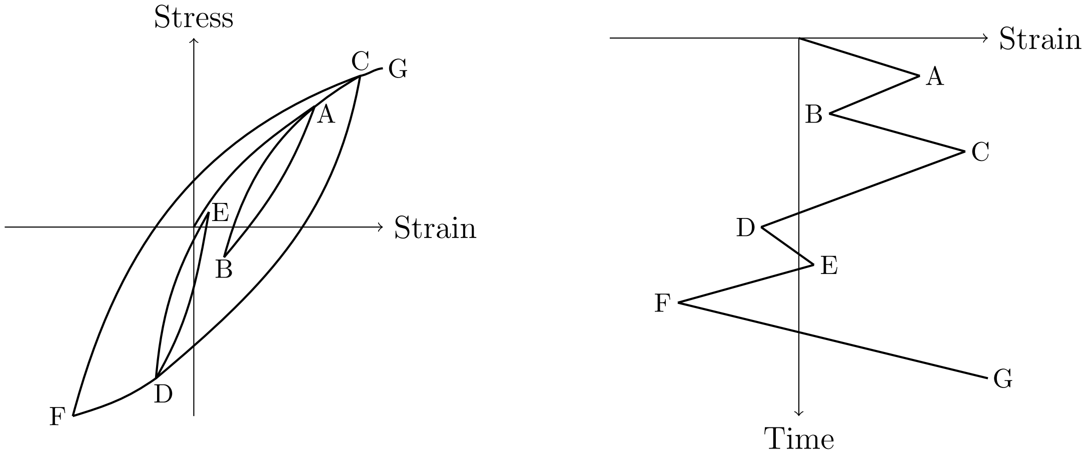

Figure 4.3: Stress/strain relation and corresponding strain history. Adapted from Anzai and Endo (1979).

Rainflow counting has obtained its name from an analogy of rain flowing off a pagoda roof. Turning a load history 90°, the method has the following rules (Almar-Næss et al., 1985):

- Rain flows from the inside of each peak or valley.
- When it reaches the next reversal, it falls down.
- The rain stops, and a cycle is completed, when it meets a flow from above.
- If the rain starts from a peak, it also stops when it comes opposite a peak of greater magnitude than the one it started from. If it starts from a valley, it stops when it comes opposite a valley of greater magnitude than the one it started from.

Figure 4.4 illustrates how these rules are applied to a given load history.

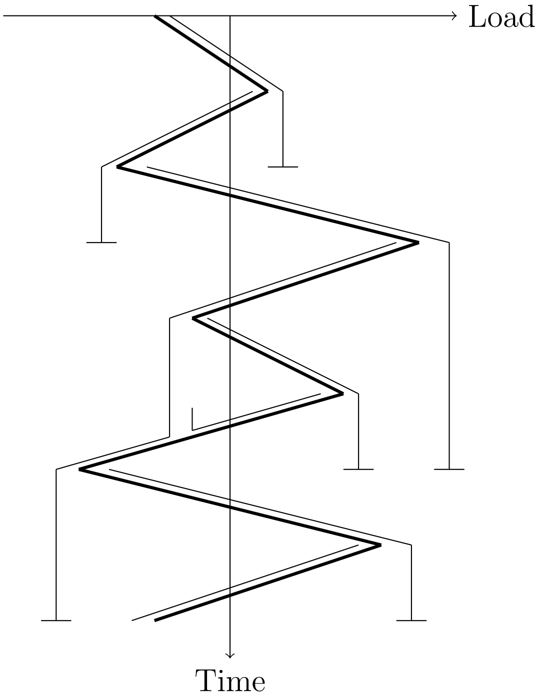

Figure 4.4: Example of rainflow.

4.5 Miner-Palmgren Summation

The most common method for calculating cumulative damage from SN data is the Miner-Palmgren summation procedure. In the method, the damage is assumed to be constant per load cycle (Almar-Næss et al., 1985)

$$D = \frac{1}{N} \tag{4.8}$$

where N is the number of cycles to failure for the given stress range. For variable amplitude loading, with k blocks of different stress ranges, the damage becomes

$$D = \sum_{i=1}^{k} \frac{n_i}{N_i} \tag{4.9}$$

with n_i being the number of load cycles in block i. The failure criterion for the structure is then

$$D_f \geq 1. \tag{4.10}$$

To reduce the probability of fatigue failure, a design fatigue factor (DFF) is often applied (DNV, 2011b). The DFF is dependent on the consequences of failure and the availability for inspection, and the failure criterion then becomes

$$DFF \cdot D_f \geq 1. \tag{4.11}$$

For fatigue failure of wellheads, a DFF = 10 is used in the analysis (DNV, 2011a).

4.6 Closed Form Fatigue Life Calculation

If the stress range distribution can be represented by a two-parameter Weibull distribution, the stress range can be written as

$$\Delta S = \Delta S_0 \left(1 - \frac{\log n}{\log n_0}\right)^{\frac{1}{h}} \tag{4.12}$$

where n is the number of cycles that exceeds ΔS, n_0 is the total number of cycles, ΔS_0 is the maximum stress range among the n_0 cycles, and h is the shape parameter of the Weibull distribution. The fatigue damage from the load history, assuming that the Miner-Palmgren hypothesis holds, can then be expressed as

$$D = \frac{n_0}{C} \frac{\Delta S_0^m}{(\ln n_0)^{\frac{m}{h}}} \Gamma\left(1 + \frac{m}{h}\right) \tag{4.13}$$

where C and m are constants from the applied SN curve, given in Eq. (4.4), and Γ is the gamma function, defined as

$$\Gamma(x) = \int_0^{\infty} e^{-t}\, t^{x-1}\, \mathrm{d}t. \tag{4.14}$$

This expression is only applicable for linear SN curves, i.e. curves with no cut-off or change in slope.

5 Soil Interaction

5.1 p-y curves

A common way to describe lateral soil-structure interaction is through p-y curves, which relates the lateral pressure from the soil (p) to the displacement of the structure (y) at a given depth. A series of nonlinear springs are then created from the curves, and attached to the structure, as illustrated in Figure 5.1.

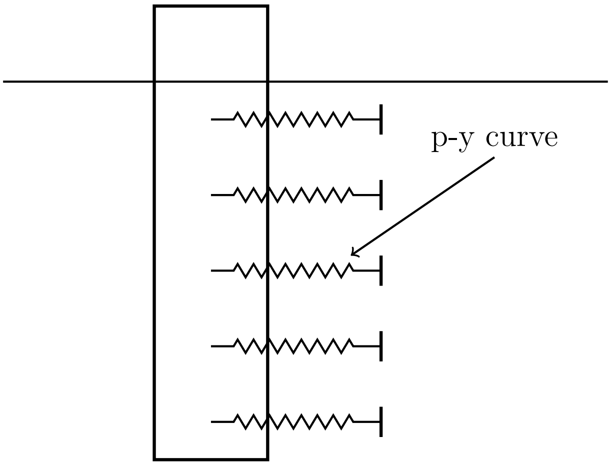

Figure 5.1: Visual representation of p-y method.

An introduction to the method can be found in Matlock (1970), who derived an empirical expression for piles in soft clay. The p-y curves for static and cyclic loads derived below is based on recommendations of API (2011), where the lateral bearing capacity is found from

$$p_u = \begin{cases} 3c + \gamma X + J\frac{cX}{D}, & X < X_R \\ 9c, & X \geq X_R \end{cases} \tag{5.1}$$

where:

p_u	Ultimate lateral resistance
c	Undrained shear strength for undisturbed clay
γ	Effective unit weight of soil
J	Dimensionless empirical constant
D	Pile diameter
X	Depth below mudline
X_R	Depth below mudline to bottom of the reduced resistance zone

If the soil strength is constant with depth, X_R can be found from the following equation:

$$X_R = \frac{6D}{\frac{\gamma D}{c} + J} \tag{5.2}$$

The p-y curves for static loads are generated from Table 5.1:

Table 5.1: p-y relation for static loads.

p/p_u	y/y_c
0.00	0.0
0.23	0.1
0.33	0.3
0.50	1.0
0.72	3.0
1.00	8.0
1.00	∞

where:

p	Lateral resistance
y	Lateral deflection
y_c	2.5 ε_cD
ε_c	Strain at one-half the maximum stress in undrained compression test

For cyclic loads, the p-y curves are generated from Table 5.2:

Table 5.2: p-y relation for cyclic loads.

$X \geq X_R$		$X < X_R$	
p/p_u	y/y_c	p/p_u	y/y_c
0.00	0.0	0.00	0.0
0.23	0.1	0.23	0.1
0.33	0.3	0.33	0.3
0.50	1.0	0.50	1.0
0.72	3.0	0.72	3.0
0.72	∞	$0.72X/X_R$	15.0
		$0.72X/X_R$	∞

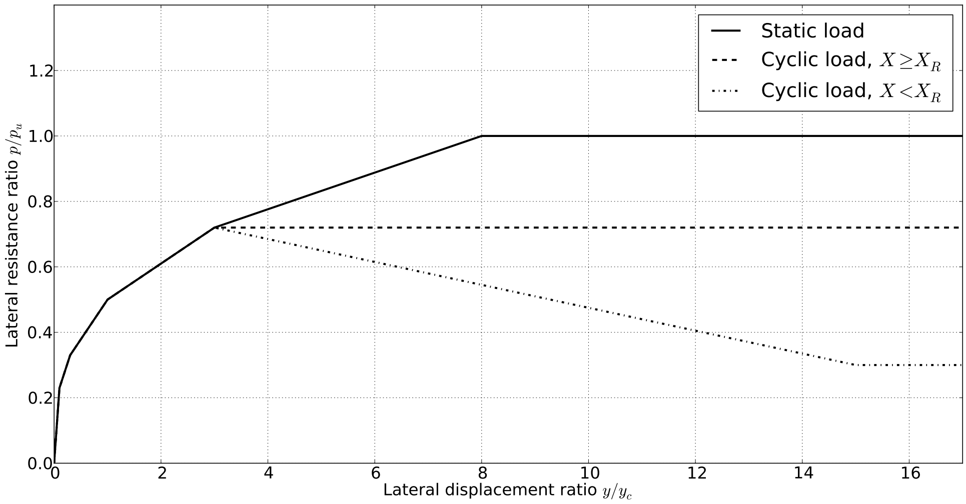

Figure 5.2: p-y curves for static and cyclic loads.

5.2 Soil Damping

There are two types of damping for a pile moving under cyclic loading. One is the hysteretic (material) damping, which is caused by shear deformations in the material. The other one is the radiation damping, which is due to energy waves being transmitted through the soil, away from the pile. For a conductor oscillating with a frequency close to the wave frequency, the radiation damping is negligible, while the hysteretic damping can be significant (Eiksund, 2014). Gazetas and Dobry (1984) showed how the hysteretic damping could be calculated for a pile in layered soils, by assuming that the average shear strain, γ, in the soil surrounding the pile can be written as

$$\gamma(z) = \frac{1+\nu}{2.5D} y(z) \tag{5.3}$$

where ν is the Poisson's ratio of the soil, D is the pile diameter, and $y(z)$ is the pile deflection. After the relation between shear strain and damping ratio is found, the distributed equivalent viscous damping coefficient can be calculated from

$$c_m(z) = 2k(z)\frac{\lambda(z)}{\omega} \tag{5.4}$$

where λ is the damping ratio, ω is the oscillating frequency, and $k(z)$ is the local secant soil stiffness, given as

$$k(z) = \frac{p(z)}{y(z)}. \tag{5.5}$$

The overall damping coefficient can then be calculated from the energy-conservation relation in classical dynamics

$$C = \int_0^L c_m(z) Y^2(z) \mathrm{d}z \tag{5.6}$$

where

$$Y(z) = \frac{y(z)}{y(0)}. \tag{5.7}$$

To find the relation between shear strain and damping ratio, a Ramberg-Osgood (R-O) model can be used to describe the nonlinear stress-strain relationship for the material. Ray and Woods (1988) concluded that this model gives a fair indication of material damping, while Kagawa (1992) showed that the model only predicts accurate damping values for parts of the shear strain range. Taken from Kagawa (1992), the following formulation is used to derive the relation:

The backbone curve for a R-O model is defined as

$$\frac{\gamma}{\gamma_r} = \frac{\tau}{\tau_{max}} \left(1 + \alpha \left| \frac{\tau}{C_1 \tau_{max}} \right|^{R-1} \right) \tag{5.8}$$

where:

τ	Shear stress
τ_{max}	Ultimate shear stress
γ_r	Reference strain, determined from the ratio τ_{max} to G_{max}
α, C_1, R	Model parameters

The relation between shear strain and shear modulus can then be expressed as

$$\left(\frac{\gamma}{\gamma_r} \right)^{R-1} = \frac{1 - \frac{G}{G_{max}}}{\alpha \left(\frac{G}{G_{max}} \right)^{R} \left(\frac{1}{C_1} \right)^{R-1}} \tag{5.9}$$

where G is the shear modulus, and G_{max} is the small-strain shear modulus. The hysteresis curves can be generated using Masing rules, where the unloading and reloading curves for a material with stress-strain relation $\tau = f(\gamma)$ is given as

$$\frac{\tau_a - \tau}{2} = f\left(\frac{\gamma_a - \gamma}{2} \right) \tag{5.10}$$

and

$$\frac{\tau_a + \tau}{2} = f\left(\frac{\gamma_a + \gamma}{2} \right), \tag{5.11}$$

respectively (see Figure 5.3). The damping ratio for a given hysteresis then becomes

$$\lambda = \frac{2}{\pi} \left(\frac{R-1}{R+1} \right) \left(1 - \frac{G}{G_{max}} \right). \tag{5.12}$$

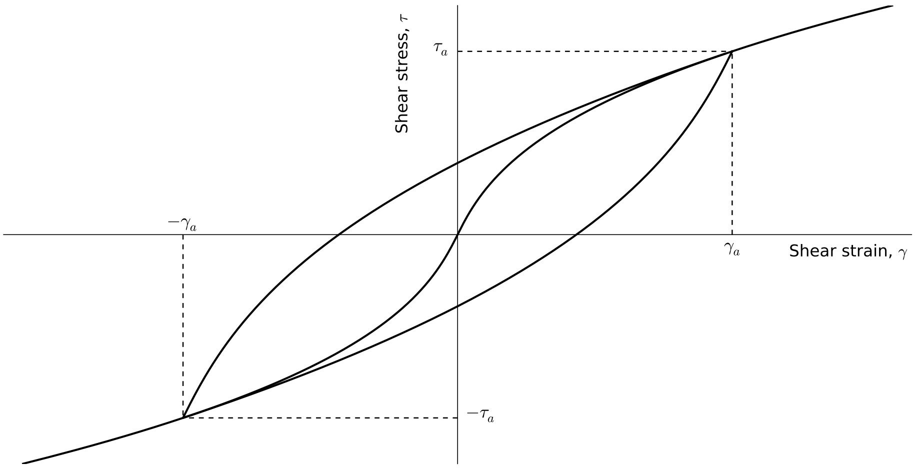

Figure 5.3: Example of R-O model with hysteresis curve.

6 Wellhead Fatigue Analysis Method

6.1 Background

In this thesis, a general wellhead fatigue analysis method proposed by DNV (2011a) is used. The method, which is summarized in the following chapter, describes how to estimate the fatigue life of a wellhead by performing two uncoupled analyses. A global analysis is performed to get a time series of the bending moment at wellhead datum, i.e. the intersection between the BOP and the wellhead. A local analysis is then used to transform the bending moments to stresses at critical hotspots. A fatigue assessment is carried out using appropriate SN curves, Miner-Palmgren summation, and stress time series from the analyses.

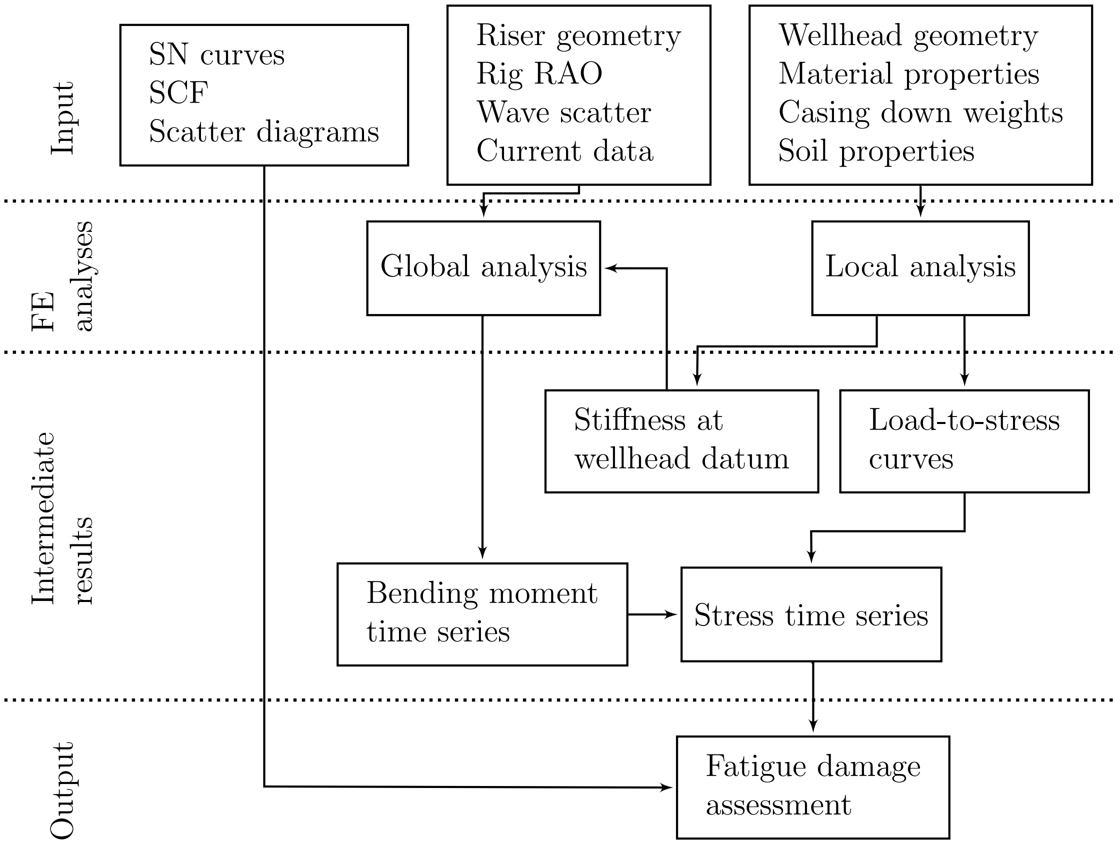

Figure 6.1: Methodology flow chart.

6.2 Local Response Analysis

6.2.1 Purpose

A local response analysis is performed in a Finite Element (FE) software. The main purpose of the local analysis is to calculate load-to-stress curves, which describe the relation between bending moment at wellhead datum and the stresses at the hotspots. In addition, the stiffness at wellhead datum is found, and used as lower boundary condition in the global analysis.

6.2.2 Model

The wellhead and conductor housing are built using solid elements. Because of symmetry about the xz-plane, only half of the model needs to be analysed, and the parts are constructed by revolving the cross-sections 180° around the vertical axis. To get accurate results at the points of interest, the surface casing and conductor are modelled with solid elements past the lowest hotspot. From there, the casings are modelled with beam elements down to approximately 50 meters below mudline, where the model is terminated and all degrees of freedom are fixed. The cement between the conductor and surface casing is fixed to the latter, and is assumed to have no friction against the conductor. The LMRP/BOP is modelled as a rigid beam, as the lateral force is applied at the location of the LFJ. To simulate the soil stiffness, nonlinear springs are made from p-y curves, and connected to the elements facing the soil. If the wellhead is installed on a template, an additional spring must be attached to the model.

6.2.3 Analysis

Stiffness at wellhead datum

Two load cases, A and B, are needed to derive the lower boundary model for the global analysis, where a simply supported beam and a nonlinear spring is used to represent the stiffness at wellhead datum, as shown in Figure 6.2.

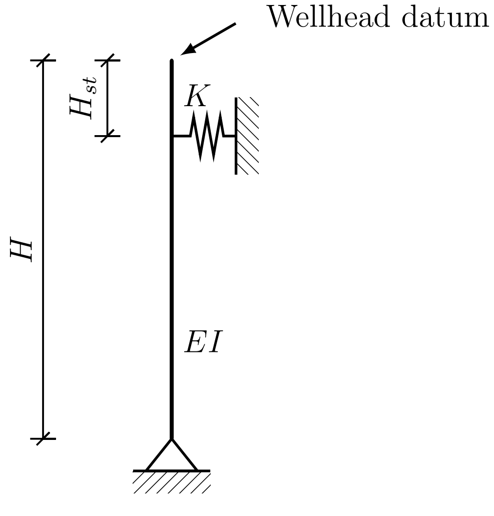

Figure 6.2: Boundary model for global analysis. Adapted from DNV (2011a).

Reinås et al. (2012) showed that this model captures the true behaviour of the well better than the coupled approach described in ISO (2010), which may not yield conservative fatigue damage estimates. The beam bending stiffness EI, the beam height H and the spring stiffness K are calculated from the analyses, while the stick-up height H_{st} is assumed to be 0.5 m.

In load case A, pure shear force is applied at the LFJ. Force/displacement and moment/rotation curves are then produced from the values at wellhead datum. In load case B, pure bending moment is applied at the LFJ, producing moment/displacement and moment/rotation curves. The two load cases describe the first two mode shapes that dominate the response (see Figure 6.3), which is required in order to get a correct representation of the system (DNV, 2011a).

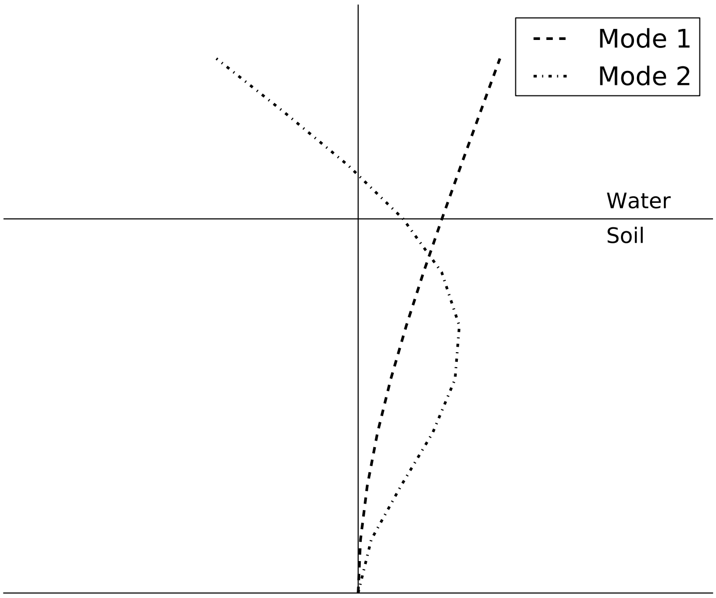

Figure 6.3: Two first dominating mode shapes for wellhead system response.

A typical point is chosen from each curve, as shown in Figure 6.4, and used to calculate the beam properties and the spring stiffness numerically (DNV, 2011a). If two values of H satisfy the equation, the most realistic value is chosen.

Transfer curves

In order to produce the load-to-stress curves, a horizontal load is applied at the LFJ, to simulate the riser response load. It is suggested that the force is increased until a bending moment of 2000 kNm is reached at wellhead datum, with an increment at every 5% of the total load (DNV, 2011a). The highest tension and compression stresses around the circumference of the hotspot are used to produce the curve. For non-welded hotspots, the von Mises stress is chosen as output, while the maximum principal stress is chosen for the welded hotspots. This is due to the reasons explained in Section 4.1.

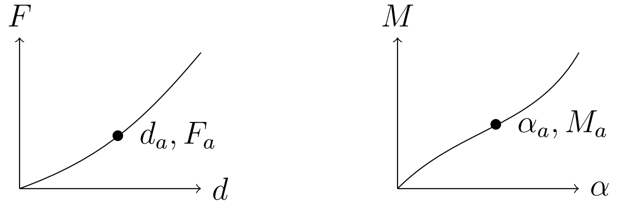

(a) Load case A, force/displacement and moment/rotation curves.

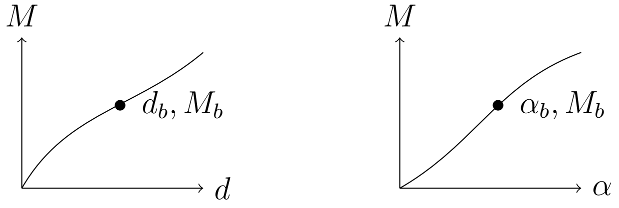

(b) Load case B, moment/displacement and moment/rotation curves.

Figure 6.4: Typical points found from the two load cases. Adapted from DNV (2011a).

6.3 Global Load Analysis

6.3.1 Purpose

A global load analysis, where the entire riser system is modelled, is performed in an appropriate software for each fundamental phase listed in Section 2.1. The purpose of the global analysis is to get time series of the bending moment at wellhead datum for all relevant sea states during the operation. The riser model should capture relevant physical effects expected to occur during the operation, and it is therefore important that the different components and their behaviour are modelled accurately.

6.3.2 Model

The different parts of the riser are modelled using beam or bar elements. The lower end is modelled as shown in Figure 6.2, with values found from the local analysis. There are several ways to model riser tension. The easiest way is to apply a point load at the upper end of the riser, but it is recommended to apply the tension through tensioners. If the riser moves in the horizontal direction, there will be a righting moment from the tensioners. If they are implemented in the model, this moment is included. It is also recommended to include the characteristics of the tensioner system, which will lead to a varying riser tension (DNV, 2011a). When the riser has a non-zero angle, θ, the tension force will have a horizontal component, T_H, which will contribute to the bending moment at wellhead datum, as shown in Figure 6.5.

Current will contribute to damping, i.e. decrease the dynamic loading on the wellhead (DNV, 2011a). A conservatively low current level, the P10 percentile, is therefore used in the method. This is a current level that is exceeded 90 % of the time. The hydrodynamic coefficients for the riser, i.e. the drag coefficient, C_D, and the inertia coefficient, C_M, are found to be 1.0 and 1.1, respectively (DNV, 2011a). The maximum projected riser diameter is used as reference diameter for the drag force. For the lower stack, C_D is also 1.0, while C_M is estimated from DNV (2012b). In both cases, the longest side of the BOP/LMRP is used as reference diameter. The flex joints should be modelled with nonlinear rotational stiffness, preferably both static and dynamic, as the secant stiffness will be non-conservative and incorrect when performing a fatigue analysis (DNV, 2011a). This is illustrated in Figure 6.6.

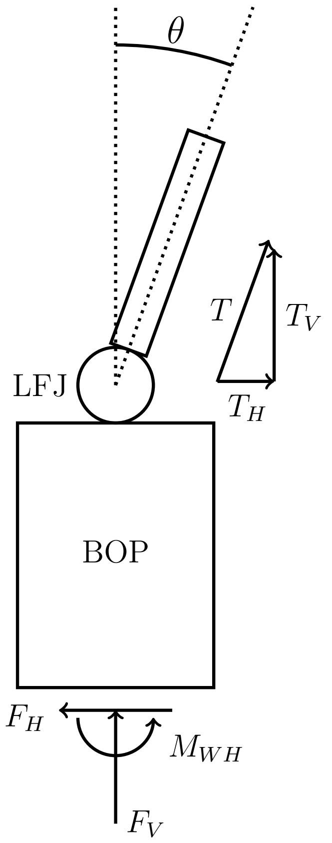

Figure 6.5: Forces on wellhead from riser tension.

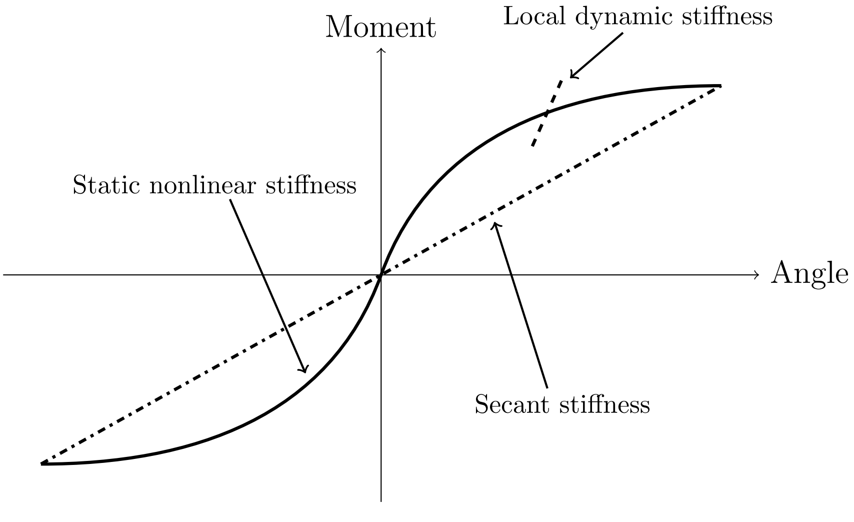

Figure 6.6: Illustration of nonlinear flex joint stiffness. Adapted from DNV (2011a).

6.3.3 Analysis

The simulations are performed in the time domain, with a simulation length of at least 3600 seconds. All wave energy is applied in one plane, i.e. long crested waves, and only one wave direction is used for all sea states. However, for historical operations, it may be considered to use directional data to variate the main wave direction (DNV, 2011a). One simulation is done for each sea state in the applied scatter diagram, and the resulting bending moment time series are used to estimate the fatigue damage, together with transfer curves found in the local analysis.

6.4 Fatigue Damage Assessment

With bending moments from the global analysis, and load-to-stress curves from the local analysis, stress histograms are created for each hotspot using rainflow counting. According to DNV (2011a), a minimum of 100 bins should be used in the stress histograms. The fatigue damage in each hotspot is then found by Miner-Palmgren summation, using appropriate SN curves. If the stress ranges follow a two-parameter Weibull distribution, the closed form expression explained in Section 4.6 can be used. The total fatigue damage in the hotspot is the sum of the damage from all phases contributing to fatigue, i.e. drilling, completion and workover, and can be written as

$$D_{total} = \sum_{Phases} D_i \tag{6.1}$$

where D_i is the damage from phase i (DNV, 2011a). There are several assumptions made in the fatigue assessment, which are summarized below:

- The bending moment and shear force at wellhead datum is the only loads contributing to fatigue.
- Welds and cross-sections have constant properties around the circumference.
- The load-to-stress curves have the same loading and unloading curve, which means that hysteresis effects are not taken into account.
- The wellhead is assumed to be perfectly vertical, and the MODU is assumed to have zero offset.

Vortex-induced vibrations (VIV) may contribute to fatigue damage, especially in locations with high currents (DNV, 2011a). However, the current analysis method does not provide guidance on how to include this effect in the calculations. The resulting fatigue damage should be reported as a function of time, where the different phases are placed in chronological order, and the most unfavourable cement level is used. The total damage for a historical or planned operation should also be reported as a function of cement level and hang-off weights, as these are uncertain parameters known to have a significant effect on the results.

7 Model and Analysis

7.1 Input

Realistic geometrical and environmental data from a North Sea well has been used as input in the analysis. Due to the sensitive nature of the information, details regarding wellhead geometry or riser component characteristics are not presented. The fatigue damage is calculated for a one year long historical operation, and evaluated in five hotspots (see Table 7.1). The locations of hotspots 1-3 are shown in Figure 7.1. Hotspot 4 and 5 are located on the conductor and surface casing, respectively, approximately 10 m below mudline. The input data only describes a drilling riser model, and the two other phases listed in Section 2.1 will therefore not be covered in the analysis.

Table 7.1: Hotspots characteristics.

	SCF	SN curve
Hotspot 1	1.2	B1
Hotspot 2	1.1	C1
Hotspot 3	1.1	F3
Hotspot 4	5.0	B1
Hotspot 5	2.0	B1

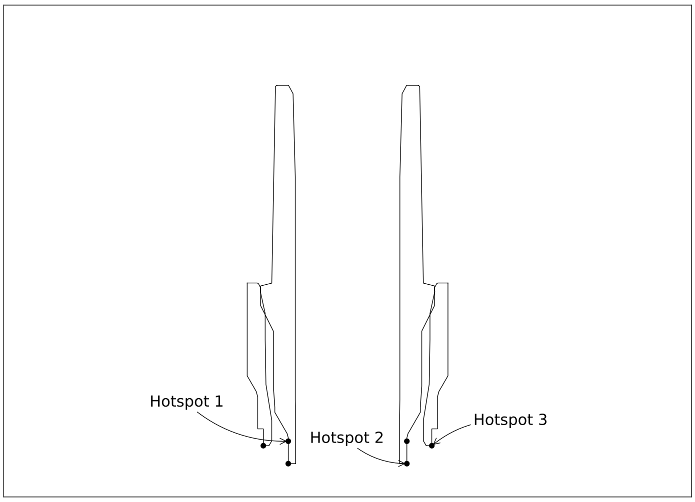

Figure 7.1: Location of hotspots 1-3.

7.2 Local Analysis

7.2.1 Wellhead Model

The wellhead is modelled and analysed in the FE program Abaqus, as described in Section 6.2.2. The system is installed on a template with a radial gap, which is accounted for by applying a translational spring at the contact point, with zero initial stiffness. The rotational stiffness of the template is not given in the input data, and is therefore not included in the analysis. The solid-beam transition and model termination are located 12 m and 70 m below mudline, respectively.

7.2.2 Simulations

The force on the LFJ is increased until the bending moment at wellhead datum reaches approximately 2000 kNm, with increments for every 5 % of the total load. The lateral displacements along the conductor at each force increment are written to file, and used to estimate the hysteretic soil damping, as described in Section 5.2. Cement shortfall is shown to have a strong effect on estimated fatigue damage, see e.g. Reinås et al. (2012). The analyses are therefore conducted with four different levels for the cement between the surface casing and the conductor: 0 m, 2 m, 5 m, and 10 m below mudline.

7.3 Global Analysis

7.3.1 Weather Data

Historical weather data for a one year long operation is used to create a scatter diagram, shown in Table 7.2, and a simulation is performed once for each cell with H_s below 6 m, which is assumed to be the cut-off limit.

Table 7.2: Applied wave scatter diagram.

H_s/T_p	3.5	4.5	5.5	6.5	7.5	8.5	9.5	10.5	11.5	12.5	13.5	14.5	15.5	16.5	17.5	18.5	Sum
0.25	0	0	0	0	0	2	0	0	0	0	0	0	0	0	0	0	2
0.75	0	3	33	50	30	24	17	6	0	0	0	0	0	0	0	0	163
1.25	1	14	50	90	130	97	79	45	19	17	5	3	2	2	2	1	557
1.75	0	3	46	60	54	74	55	50	41	20	12	2	6	1	0	1	425
2.25	0	1	6	48	48	36	32	41	43	39	19	9	6	4	0	0	332
2.75	0	0	0	19	49	32	42	56	59	46	14	11	6	0	0	0	334
3.25	0	0	0	6	32	52	19	31	48	21	17	7	6	2	0	0	241
3.75	0	0	0	1	12	32	43	29	18	25	12	10	3	7	1	0	193
4.25	0	0	0	0	8	35	37	15	18	10	16	7	3	1	0	0	150
4.75	0	0	0	0	0	13	23	22	19	14	12	3	2	1	0	0	109
5.25	0	0	0	0	0	8	13	24	8	13	12	5	4	0	1	0	88
5.75	0	0	0	0	0	3	5	10	6	7	6	9	5	0	1	1	53
Sum	1	21	135	274	363	408	365	329	279	212	125	66	43	18	5	3	2647

Only one wave heading is used for all analyses, when in reality, each sea state has its own main wave direction. As the system is nearly axisymmetrical, changes in fatigue damage for different headings will be caused by the fact that the motions of the MODU vary with the relative wave direction. The most important MODU motions for wellhead bending moment are the translations in the horizontal plane, i.e. surge and sway (Larsen, 2013). All analyses are performed with a wave heading relative to the MODU of both 0° (head sea) and 90° (beam sea), to investigate the significance of the main wave heading. In Figure 7.2 and 7.3, the Response Amplitude Operator (RAO) and phase angle are shown for surge and sway for the two wave headings. The values on the y-axes have been removed on request.

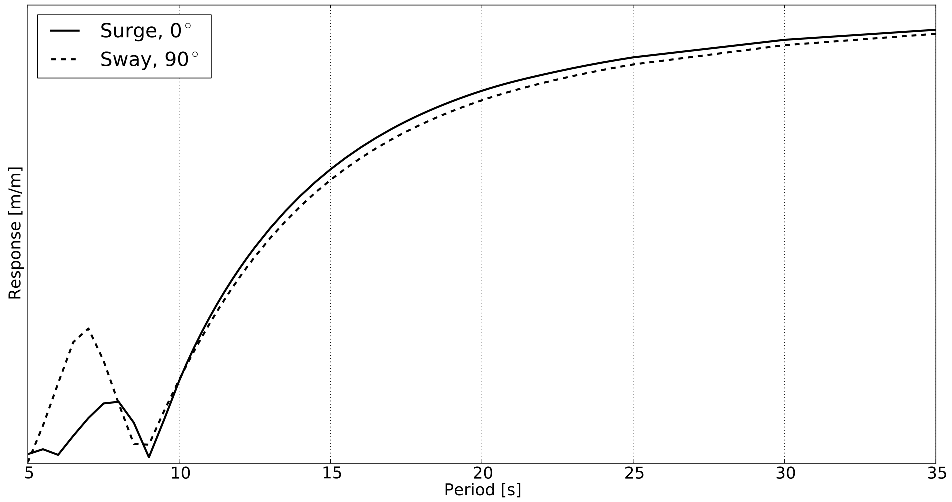

Figure 7.2: RAO for surge, head sea and sway, beam sea.

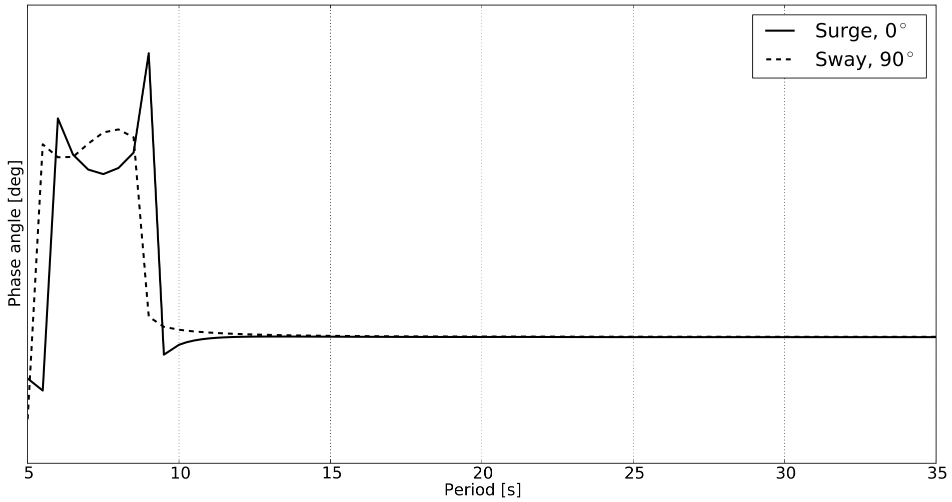

Figure 7.3: Phase angle for surge, head sea and sway, beam sea.

7.3.2 Riser Model

The global analysis is conducted in Sima/Riflex, a software for analysis of slender marine structures developed by MARINTEK. In real life, there will be a variation in riser top tension, due to friction and fluid drag in the tensioner system (Holm et al., 2013). The varying tension force can be written (Larsen, 2013)

$$T(t) = T_{avg} + c\Delta\dot{z}(t) + k\Delta z(t) \tag{7.1}$$

where T_{avg} is the average tension, $\Delta z(t)$ is the deviation from average stroke length, and $\Delta\dot{z}(t)$ is the stroke velocity. c and k are the damping and stiffness coefficients of the system, respectively. To simplify the model, tension variation is neglected, and a constant tension equal to the tension at average stroke length is applied to the tensioners. Modelling aspects which should be noted are:

- The water depth at the drilling site is 139.5 m.
- The BOP and the LMRP, which have a rectangular cross section in the input data, are modelled with an external diameter equal to the longest side.
- The added mass coefficient for the lower stack is found from DNV (2012b) to be 1.51.
- To simulate the slip joint, where the inner barrel slides into the outer barrel, the former is modelled as a bar element with very low axial stiffness.
- The flex joints are modelled with nonlinear stiffness, which is given in the input data.
- Drilling mud with a density $\rho_{mud} = 1400$ kg/m^3 is applied inside the pipes.
- The six tensioners are modelled as bar elements with constant axial force regardless of elongation. The lower nodes in the tensioner elements are slaved to the tension ring node, while the upper nodes are fixed to the MODU.

7.3.3 Simulations

The simulations are performed in the time domain, with long crested waves and a simulation length of 3600 seconds. Grytøyr and Steinkjer (2012) showed how the uncertainty in long term fatigue damage decreases as the simulation length increases, and recommended a minimum simulation length of 600 seconds. A simulation length of 3600 seconds is therefore considered to be sufficient. A three parameter JONSWAP spectrum is used to describe the waves, where H_s, T_p and γ are input parameters. The peakedness parameter, γ, is found from (MARINTEK, 2013*b*)

$$\gamma = \begin{cases} 1.0, & T_p \geq 5.0\sqrt{H_s} \\ e^{5.75-1.15T_pH_s^{-0.5}}, & 3.6\sqrt{H_s} \leq T_p < 5.0\sqrt{H_s} \\ 5.0, & T_p < 3.6\sqrt{H_s}. \end{cases} \tag{7.2}$$

The wave time series is found by FFT, and linear wave theory is applied. For the numerical integration, the Newmark-β method with $\beta = {}^1/_4$ and $\gamma = {}^1/_2$ is used. This corresponds to the constant average acceleration method, shown in Figure 3.6b. The stiffness proportional Rayleigh damping coefficient, α_2, is chosen so that the system gets a critical damping ratio of 0.1 % with respect to the first eigenfrequency of the riser system.

7.4 Fatigue Damage Assessment

The bending moment time series are converted to stress time series for all hotspots and cement levels using the load-to-stress curves found in the local analysis. Stress histograms for each sea state is then produced using the rainflow cycle counting procedure through the WAFO package (Brodtkorb et al., 2000) in Matlab. In order to get the total damage for the operation, a long term stress histogram is created from a weighted sum of the short term histograms. The weight factors are the probability of occurrence for each sea state, found from the scatter diagram (see Table 7.2). The historical weather data is used to find the damage as a function of time, as well as to find the distribution of damage around the circumference of the hotspots.

7.5 Diffraction Effects

For a standard global riser analysis, the undisturbed incoming wave is used to calculate fluid velocities and accelerations along the riser. However, the presence of a large structure will cause disturbance, which can lead to changes in the fluid kinematics in the area of the riser. The disturbed fluid kinematics for a given point can be found from a sink-source computer program, and applied in the global analysis in Sima/Riflex.

A simplified FE model of an Aker H6 semi-submersible, shown in Figure 7.4, is imported into the DNV software Wadam. The transfer functions for pressure and particle velocity in given points are found from the radiated and diffracted wave field, using potential theory (DNV, 2013). The riser is assumed to be placed in the center of the platform, i.e. in (x,y) = (0,0), and the coordinate system is defined such that 0° (head sea) waves are propagating along the x-axis. The transfer functions are extracted for each meter down to 30 meters below mean surface, where the kinematics are assumed to be unaffected by the structure.

The transfer functions for the diffracted wave kinematics, which are taken into Sima/Riflex, are defined as

$$H_{\eta^d}(\beta,\omega) = \frac{\eta^d(\beta,\omega)}{\zeta_a(\beta,\omega)} \tag{7.3}$$

and

$$H_{u_j^d}(\beta,\omega) = \frac{u_j^d(\beta,\omega)}{\zeta_a(\beta,\omega)}, \tag{7.4}$$

where η^d is the diffracted wave elevation, ζ_a is the amplitude of the incoming wave, β is the propagation direction of the incoming wave, ω is the wave frequency, and u_j^d is the diffracted wave velocity, where j = 1,2,3 equals x, y and z direction (MARINTEK, 2013*a*). The transfer functions for the fluid particle accelerations are calculated in Sima/Riflex, based on the velocity transfer functions, while the kinematics for intermediate nodes are found by interpolation.

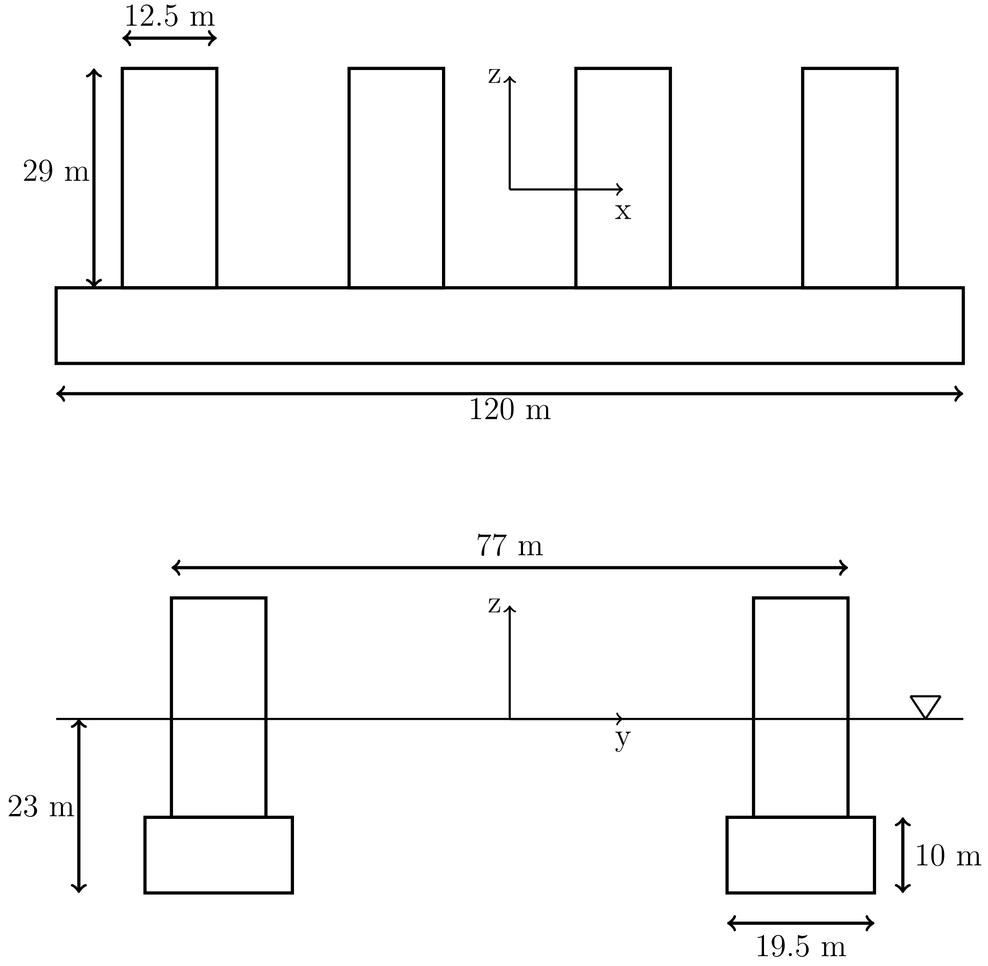

Figure 7.4: Simplified model of an Aker H6 semi-submersible.

Wadam reports transfer functions for pressure instead of wave elevation. The wave elevation is therefore obtained from potential theory as

$$\eta = \frac{p}{\rho g} \tag{7.5}$$

where p is the pressure at mean water level (DNV, 2013).

7.6 Soil Stiffness and Damping

The analyses are run with both static and cyclic p-y curves, which are derived from a soft clay with soil parameters given in Table 7.3.

Table 7.3: Soil properties.

Parameter	Symbol	Value
Undrained shear strength	c	20 kPa
Effective unit weight	γ	21.3 kN/m^3
Strain at 50 % strength	ε_{50}	1.0 %
Small strain shear modulus	G_{max}	10.0 MPa
Poisson's ratio	ν	0.4

Soil damping is estimated as a function of oscillation frequency and lateral displacement at mudline, using an R-O model and the displacements along the conductor found from Abaqus. The R-O model parameters vary with different soils, and should ideally be found from curve fitting. Since empirical values for shear modulus or damping ratio at different strain levels are not available, the parameters are taken from Kagawa (1992), and shown in Table 7.4.

Table 7.4: R-O model parameters.

Parameter	Value
α	1.0
C_1	0.5
R	1.7

This gives a strain-damping relationship as shown in Figure 7.5.

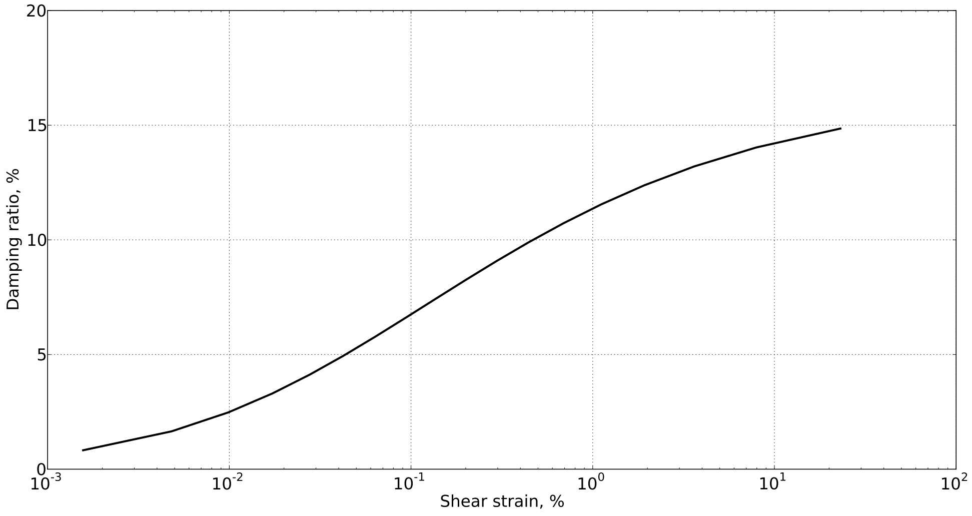

Figure 7.5: Damping curve from R-O model.

Since Sima/Riflex only supports constant damping coefficients, a characteristic displacement and frequency have to be selected for each sea state. For the oscillating frequency, the first eigenfrequency of the riser system is chosen, while the displacement corresponding to the most critical stress amplitude in the base case is selected as the characteristic displacement. The most critical stress amplitude is here defined as the stress range which contributes most to the fatigue damage in each sea state, divided by two. The mean and standard deviation of the damping ratios relative to critical damping for each sea state are shown for head and beam sea in Table 7.5.

Table 7.5: Damping ratio mean and standard deviation.

	Head sea	Beam sea
Mean	9.34 %	8.39 %
Standard deviation	1.55 %	1.46 %

7.7 Drag Coefficient

When calculating the drag forces on the riser, the projected diameter of the main tube with auxiliary lines is used as hydrodynamic diameter. However, since a riser with external auxiliary lines is not axisymmetric, the projected diameter will change during an operation. In DNV (2011a), the maximum projected diameter is used in all analyses, and the nondimensional drag coefficient, C_D, is found to be equal to 1.0. Here, the analyses are also run with a hydrodynamic diameter equal to the projected diameter for a flow perpendicular to the one giving maximum drag, while C_D is held constant. The hydrodynamic diameter may then be written as

$$D_h = D_{riser} + D_{bst}. \tag{7.6}$$

This is illustrated in Figure 7.6, where D_{max} and D_{perp} are the hydrodynamic diameters from Eq. (3.25) and (7.6), respectively.

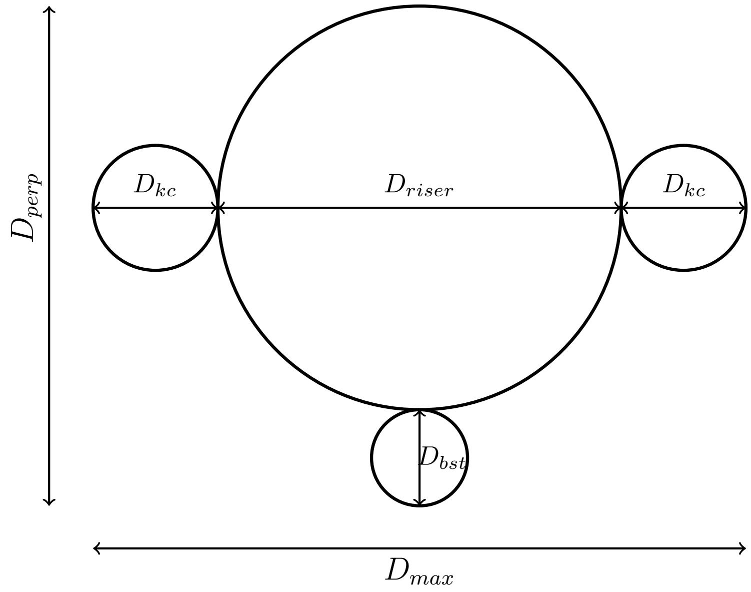

Figure 7.6: Riser joint configuration.

The hydrodynamic diameter, and therefore also the drag force per unit length of the riser, is reduced by 23.5 % when using D_{perp} instead of D_{max}.

7.8 Wave Directionality

During an operation, the main wave direction will change, which means that the point on the circumference of the hotspot with the most load will vary. If unidirectional waves are applied, the stress at an arbitrary point B on the circumference is

$$\sigma_B = \sigma_A \cos(\theta) \tag{7.7}$$

where σ_A is the stress in the point with most load, and θ is the angle between B and the wave direction. This is illustrated in Figure 7.7.

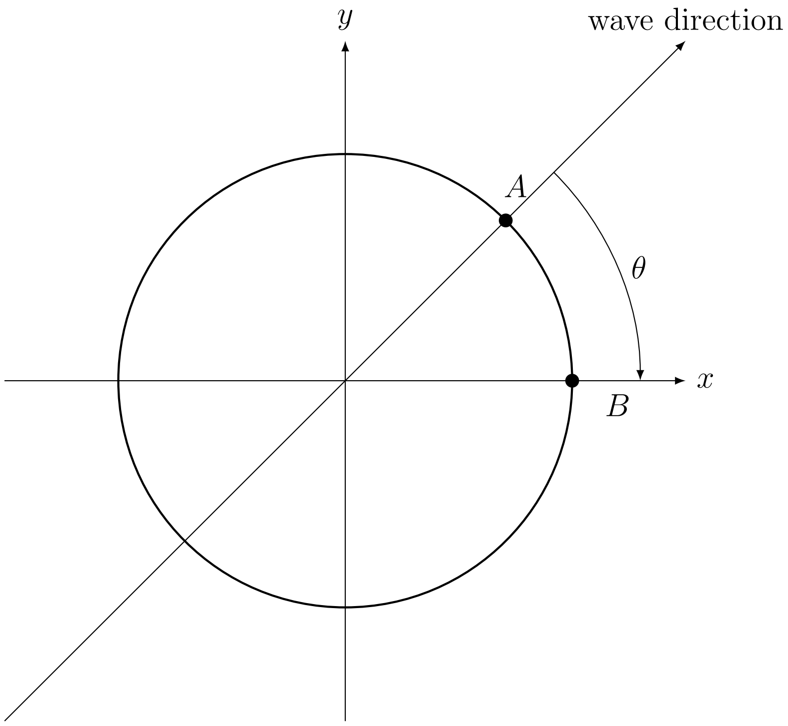

Figure 7.7: Wave loading on pipe cross-section.

Directional data from the input is used to investigate the effect of spreading the fatigue damage around the circumference of the hotspot. It should be noted that only one wave heading is used for all sea states in the global analysis, and that the wave directionality is only accounted for in the fatigue assessment. The results are therefore only valid for RAOs which are independent from wave heading, something which is not the case. It could, however, give an indication of the effect wave directionality has on fatigue damage. The distribution of wave directions during the operation is shown in Figure 7.8.

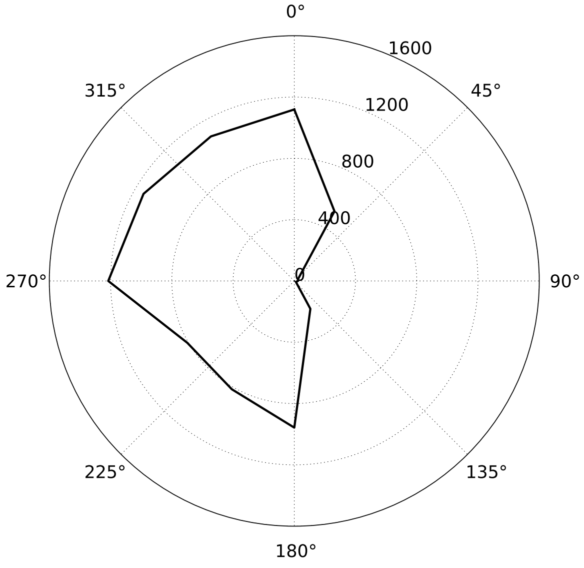

Figure 7.8: Distribution of wave directions for the operation (hours).

The fatigue damage is calculated for 12 points around the circumference of the hotspot, as shown in Figure 7.9. Because of symmetry, only the points 1-6 need to be analysed.

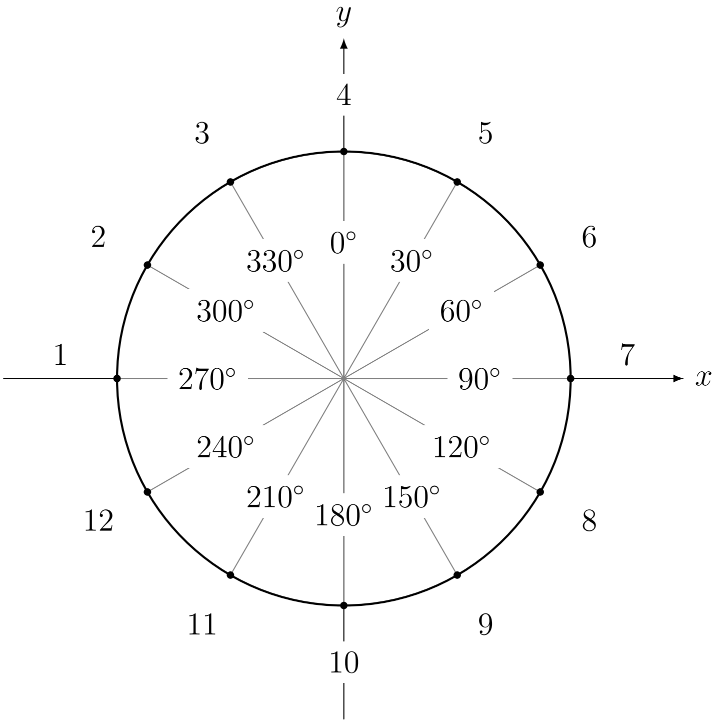

Figure 7.9: Analysed points at each hotspot.

8 Results and Discussion

8.1 Local Analysis

Figure 8.1 shows the displacements of upper part of the conductor for different increments of the maximum load, which corresponds to a bending moment of approximately 2000 kNm at wellhead datum. The vertical line at $3.0\,y_c = 0.06858$ m is the displacement where the cyclic p-y curves starts to differ from the static p-y curves (see Figure 5.2). It is therefore the minimum displacement needed in order to get an effect from the alternative soil spring modelling. It can be seen from the figure that the displacement is lower than $3.0\,y_c$ for all points and load increments, and the cyclic p-y curves will therefore give the exact same result as the static p-y curves. Load-to-stress curves are also created for all hotspots and cement levels, and can be found in Appendix A.

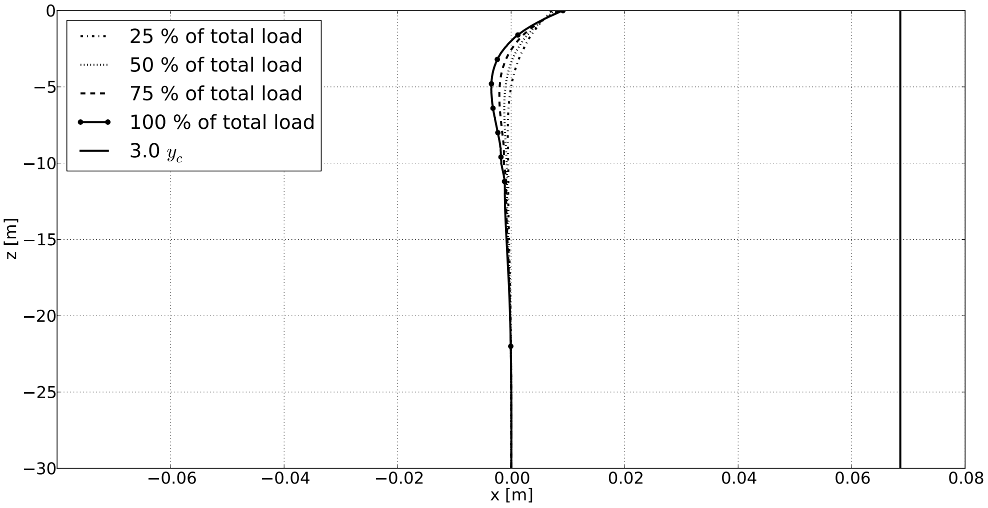

Figure 8.1: Conductor displacements for different load increments.

The parameters used to express the stiffness at wellhead datum in the global analysis (see Figure 6.2), i.e. the beam height H and stiffness EI, and spring stiffness K, are calculated from the results in the local analysis, and shown in Table 8.1 and Figure 8.2, respectively.

Table 8.1: Lower boundary model parameters.

Parameter	Value
Height, H	4.76 m
Bending stiffness, EI	$3.22 \cdot 10^8$ Nm^2

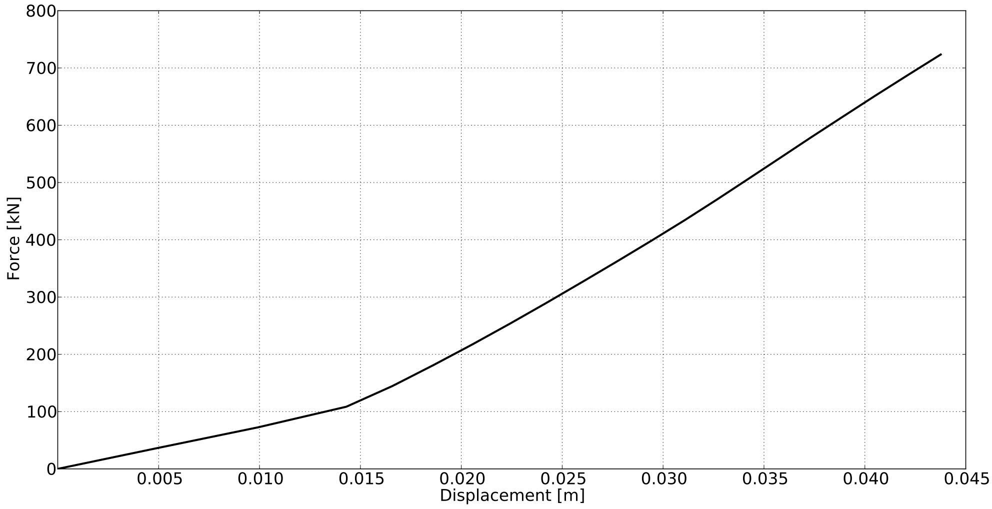

Figure 8.2: Force-displacement curve for the equivalent soil spring.

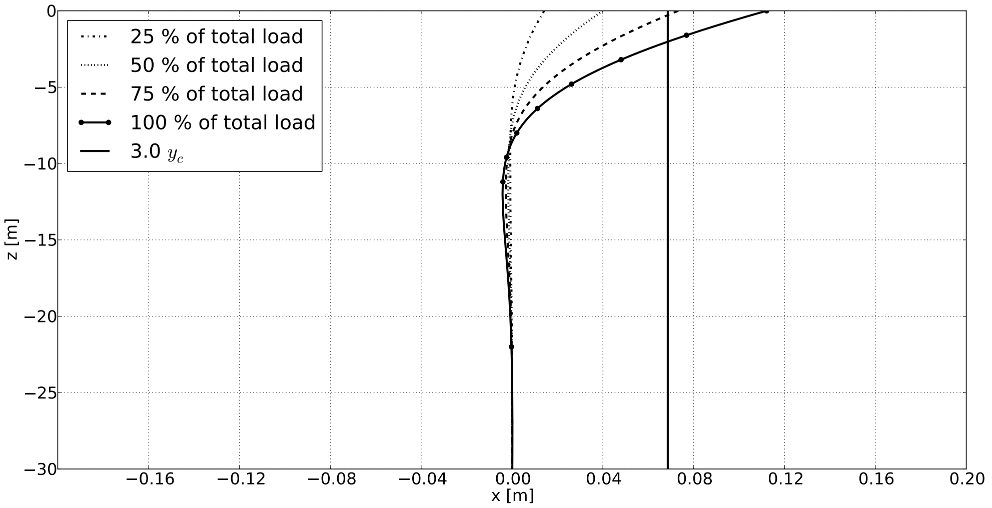

Figure 8.3: Conductor displacements for different load increments without template support.

The soil spring has a sudden increase in stiffness at a reaction force of approximately 100 kN. At this point, the radial gap between the conductor and the template is closed, and the template spring contributes to the stiffness of the system. If the template support is removed, the soil springs will take all the lateral load, and the stiffness of the system is reduced. Consequently, the upper part of the conductor displaces more than $3.0\,y_c$ under large lateral loads, as shown on Figure 8.3, and the choice of p-y curves will affect the response of the system. The consequence is, as expected, a slightly softer equivalent soil spring for cyclic p-y curves under large displacements, shown in Figure 8.4. This is caused by the decrease and stagnation in reaction force which the cyclic soil springs experience when a lateral displacement of $3.0\,y_c$ is reached.

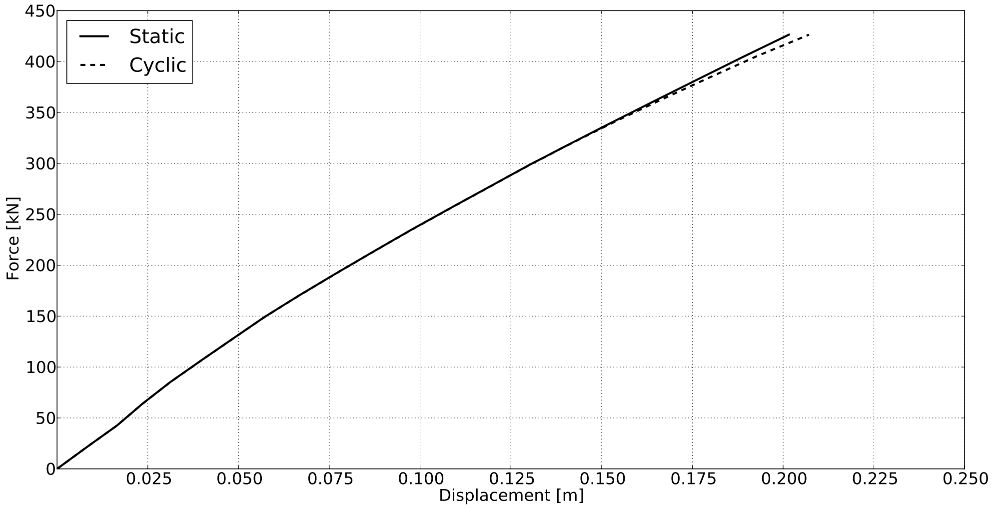

Figure 8.4: Force-displacement curve for the soil spring without template support.

The effect of using cyclic p-y curves is also visible in the transfer curves. Cyclic curves will give a softer soil for the upper part of the conductor, which results in larger stresses in the lower hotspots. This can be seen in Figure 8.5, where the stresses in hotspot 4 is slightly higher for cyclic soil springs. An opposite effect is expected for the hotspots closest to mudline, however, the difference is negligible.

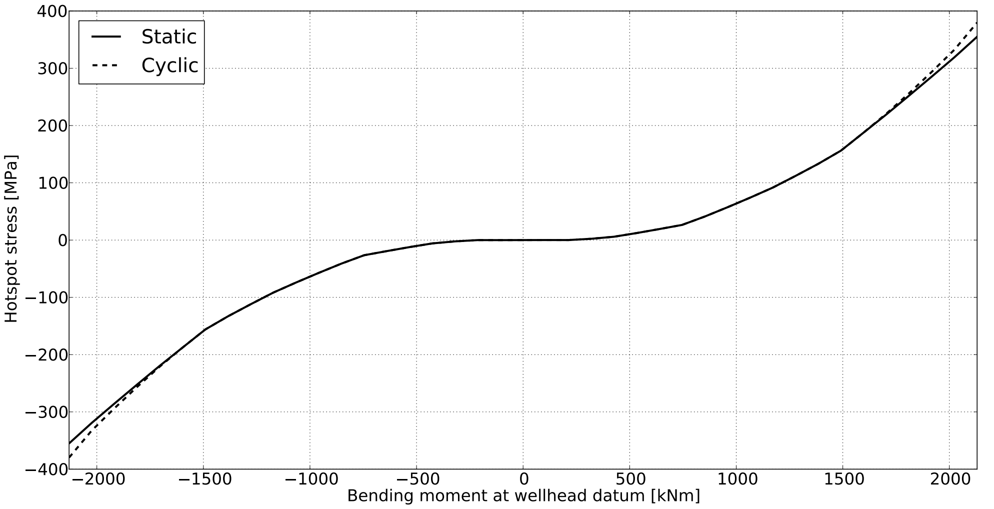

Figure 8.5: Load-to-stress curve for hotspot 4, 10 m cement shortfall without template support, static and cyclic p-y curves.

8.2 Global Analysis

Table 8.2 and 8.3 show the standard deviation and maximum bending moment at wellhead datum for each sea state with one hour simulation time. Both standard deviation and maximum bending moment increases, as expected, when H_s increases. It can be seen from the tables that $T_p = 8.5$ s gives the largest standard deviation for all significant wave heights, and also the largest maximum for most. This is close to the first eigenperiod of the riser at 9.5 s, and coincides with the local maxima in surge amplitude, see Figure 7.2.

Table 8.2: Bending moment standard deviation (kNm) at wellhead datum, one hour simulation, head sea.

H_s/T_p	3.5	4.5	5.5	6.5	7.5	8.5	9.5	10.5	11.5	12.5	13.5	14.5	15.5	16.5	17.5	18.5
0.25	0	0	0	0	0	21.75	0	0	0	0	0	0	0	0	0	0
0.75	0	42.47	52.43	56.17	62.54	65.57	64.06	59.55	0	0	0	0	0	0	0	0
1.25	37.28	69.68	87.24	94.93	101.84	107.56	106.84	96.08	88.92	78.14	72.86	66.04	57.61	52.61	47.29	43.33
1.75	0	100.62	140.16	131.06	147.13	153.42	145.88	138.68	127.03	113.86	100.95	91.55	81.63	73.33	0	60.10
2.25	0	131.38	199.33	166.84	184.84	194.61	190.75	176.11	157.72	143.30	129.59	114.42	105.67	166.84	0	0
2.75	0	0	0	199.22	228.31	232.70	218.77	208.99	188.74	176.42	152.58	140.82	123.79	0	0	0
3.25	0	0	0	236.50	269.17	283.29	260.29	238.13	223.46	203.37	182.67	163.87	149.43	129.86	0	0
3.75	0	0	0	275.02	309.43	326.09	301.34	279.56	260.89	231.13	202.88	185.88	166.30	146.40	136.22	0
4.25	0	0	0	0	344.92	377.43	343.77	313.87	274.46	259.73	233.59	208.76	190.44	169.98	0	0
4.75	0	0	0	0	0	419.04	371.99	338.61	312.23	281.74	252.79	226.51	210.12	189.18	0	0
5.25	0	0	0	0	0	452.24	404.96	353.82	340.19	313.07	280.18	256.05	226.65	0	188.41	0
5.75	0	0	0	0	0	490.94	450.10	377.00	356.62	338.39	306.46	272.87	246.08	0	204.08	185.86

Table 8.3: Maximum bending moment (kNm) at wellhead datum, one hour simulation, head sea.

H_s/T_p	3.5	4.5	5.5	6.5	7.5	8.5	9.5	10.5	11.5	12.5	13.5	14.5	15.5	16.5	17.5	18.5
0.25	0	0	0	0	0	90.18	0	0	0	0	0	0	0	0	0	0
0.75	0	159.30	214.08	254.52	253.86	265.18	228.89	220.07	0	0	0	0	0	0	0	0
1.25	138.37	285.84	368.86	422.02	575.14	445.63	609.11	345.55	446.20	311.82	318.55	246.46	286.29	189.84	174.16	167.60
1.75	0	510.41	678.92	573.72	661.78	748.73	655.10	619.85	520.16	417.36	374.40	348.27	326.90	307.11	0	269.86
2.25	0	926.06	806.87	725.44	806.37	838.96	807.35	687.91	643.95	628.37	557.63	468.75	406.29	725.44	0	0
2.75	0	0	0	847.72	899.14	1106.98	968.48	887.08	774.11	719.28	669.04	558.59	447.73	0	0	0
3.25	0	0	0	984.29	1163.49	1182.55	1181.33	896.75	877.86	1037.20	815.55	611.66	611.93	522.77	0	0
3.75	0	0	0	1132.29	1228.89	1464.82	1133.04	1102.06	1018.77	894.28	861.32	743.21	690.79	609.28	612.39	0
4.25	0	0	0	0	1466.58	1481.89	1234.85	1288.96	1104.73	907.94	951.89	799.59	787.46	692.13	0	0
4.75	0	0	0	0	0	1442.12	1485.12	1309.49	1335.58	1175.53	957.78	985.73	917.02	811.15	0	0
5.25	0	0	0	0	0	1639.90	1600.59	1321.38	1393.56	1294.33	1104.42	951.98	975.94	0	868.89	0
5.75	0	0	0	0	0	2012.18	1774.16	1598.27	1342.71	1345.72	1197.66	970.36	905.82	0	865.20	729.72

In Figure 8.6, the standard deviation of the bending moment at wellhead datum is plotted against T_p for head and beam sea when $H_s = 1.25$ m. The standard deviation is significantly larger in beam sea for peak periods where the sway amplitude is higher than the surge amplitude. The maximum standard deviation for beam sea is seen to coincide with the local maxima in sway amplitude, which also applies for surge in head sea. It should be noted that there is also a relatively great difference between head sea and beam sea at higher T_p, where most of the energy is in wave periods where the amplitudes in surge and sway are nearly identical. This applies for all significant wave heights, and indicates that the difference in surge/sway amplitude for wave periods between 5-8 seconds has a significant impact on the bending moment at wellhead datum.

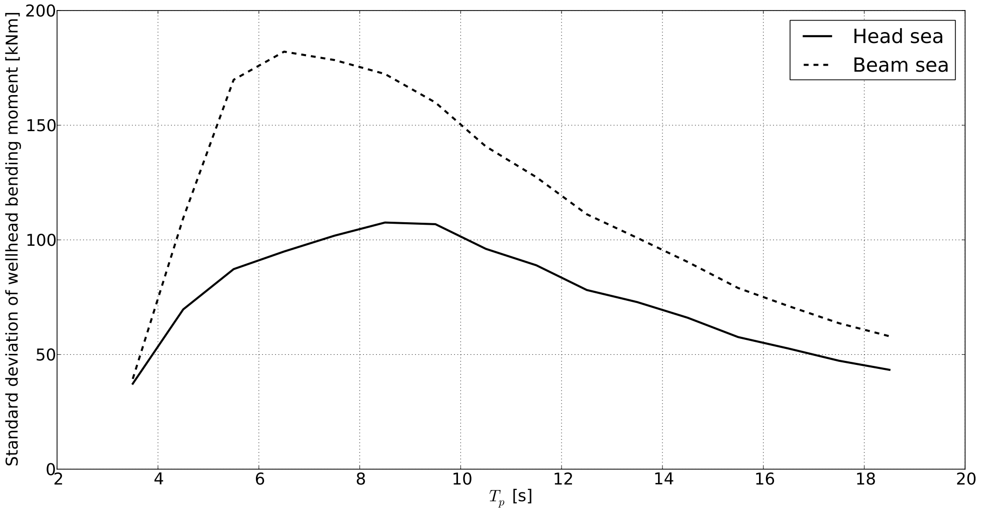

Figure 8.6: Bending moment standard deviation at wellhead datum, $H_s = 1.25$ m.

The consequence of this is that the beam sea analysis yields a much higher cycle count than the head sea analysis, especially for high moment ranges. This is shown in Figure 8.7.

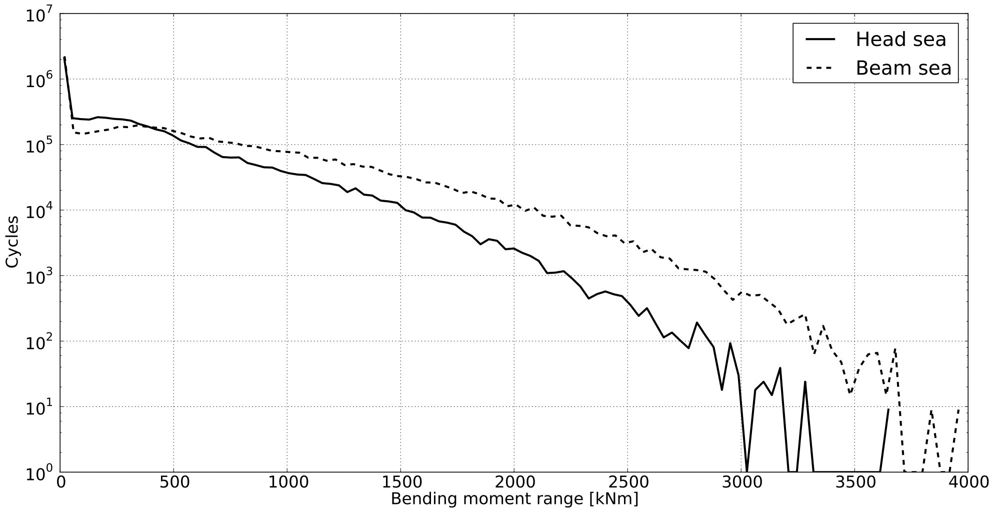

Figure 8.7: Weighted bending moment histogram for the whole operation, head sea and beam sea.

Figure 8.8 shows the weighted bending moment histogram for static and cyclic p-y curves when the template support is removed. The curves are nearly identical, but a small decrease in load cycles can be seen for the slightly softer cyclic spring in the high load area.

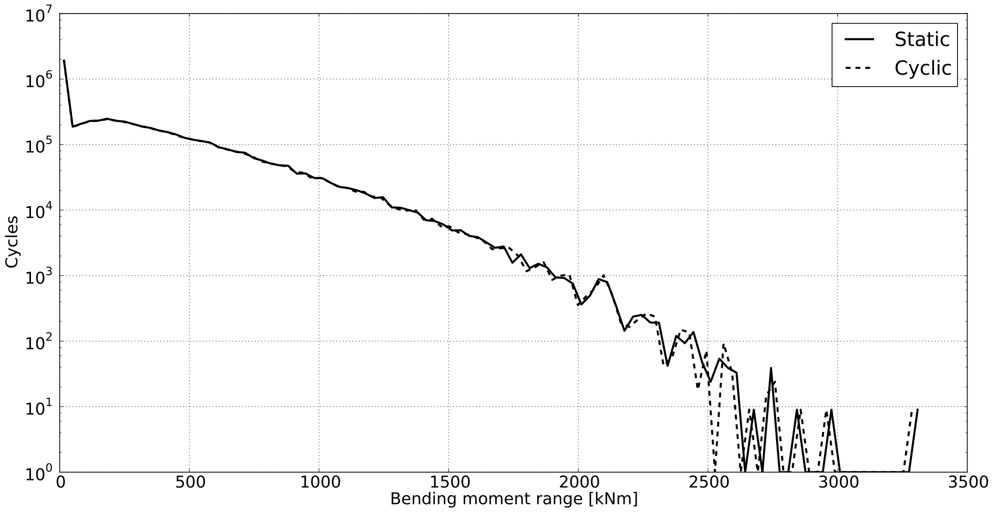

Figure 8.8: Weighted bending moment histogram for the whole operation without template support, static and cyclic p-y curves.

In Figure 8.9 and 8.10, the standard deviation of the bending moment at wellhead datum is shown for $H_s = 4.25$ m for four different cases in head and beam sea, respectively. Both figures show that soil damping gives a reduction in the standard deviation which is nearly independent of T_p. This is also the case for the higher standard deviation due to a reduced drag diameter. Including diffraction from the MODU in the analysis is expected to have a different effect for head sea than for beam sea, as the structure disturbing the incoming wave is different for the two directions (see Figure 7.4). For head sea, diffracted kinematics lead to a decrease in bending moment for low spectral peak periods, while the curves are identical for higher T_p. For beam sea, however, the diffracted kinematics give a slightly higher standard deviation than the base case for all peak periods.

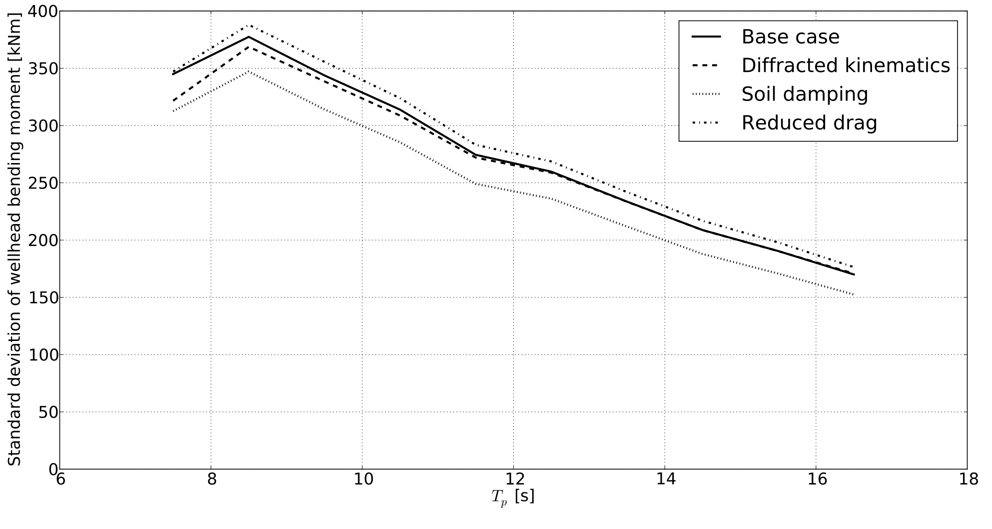

Figure 8.9: Bending moment standard deviation at wellhead datum, $H_s = 4.25$ m, head sea.

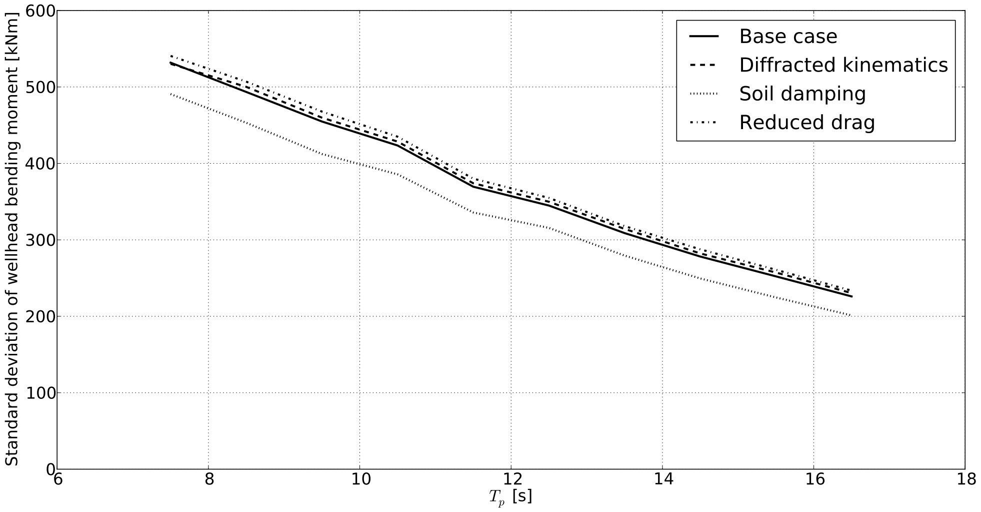

Figure 8.10: Bending moment standard deviation at wellhead datum, $H_s = 4.25$ m, beam sea.

8.3 Fatigue Damage Assessment

The fatigue damage resulting from the operation is estimated for five hotspots and four different cement levels. The total damage, normalized with respect to the most critical hotspot and cement shortfall, is shown as a function of cement level in Figure 8.11a and 8.11b.

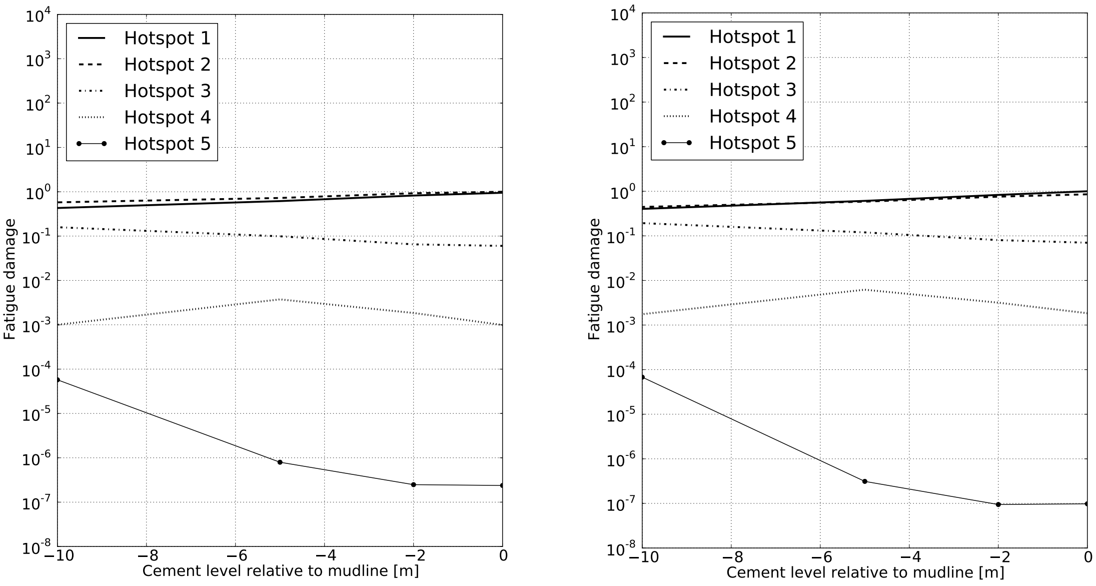

(a) Head sea. **(b)** Beam sea.

Figure 8.11: Total fatigue damage normalized with respect to most critical hotspot and cement level.

The figures show that the hotspots on the wellhead itself, i.e. hotspot 1 and 2, are the most critical ones with respect to fatigue failure, and that the relative difference between them is marginal. The figures also show that cementing all the way up to mudline yields the shortest fatigue life. This is due to less load transfer down the conductor and surface casing, which can be seen on the fatigue damage for hotspot 3, 4 and 5. Hotspot 5, which is located on the surface casing approximately 10 m below mudline, is the hotspot most affected by a change in cement level, and a cement shortfall of 10 m results in 241 and 713 times shorter fatigue life compared to cement up to mudline. This stresses the importance of conducting analyses with a wide range of cement levels.

Table 8.4 shows the difference in estimated fatigue damage between head sea and beam sea for the unidirectional waves in the global analysis, normalized with respect to head sea damage. There is a significant increase in fatigue damage when beam sea waves are applied, which is expected considering the cycle count in Figure 8.7. One wave heading is usually applied for all sea states in future operations, and it is stated in DNV (2011a) that the most unfavourable direction should be used if an operation is planned for an existing structure. The results show that using directional data could reduce the estimated damage significantly, however, this does not necessarily yield conservative results on fatigue life.

Table 8.4: Total fatigue damage normalized with respect to head sea, worst cement level.

	Head sea	Beam sea
Hotspot 1	1.00	3.37
Hotspot 2	1.00	2.74
Hotspot 3	1.00	3.89
Hotspot 4	1.00	5.31
Hotspot 5	1.00	3.78

The unweighted and weighted distribution of the estimated fatigue damage for the operation can be found in Table 8.5 and 8.6, respectively. The unweighted fatigue damage distribution is seen, as expected, to have a strong correlation with the standard deviation of bending moment at wellhead datum.

Table 8.5: Distribution (%) of unweighted fatigue damage in most critical hotspot for worst cement level, head sea.

H_s/T_p	3.5	4.5	5.5	6.5	7.5	8.5	9.5	10.5	11.5	12.5	13.5	14.5	15.5	16.5	17.5	18.5	Sum
0.25	0	0	0	0	0	0.00	0	0	0	0	0	0	0	0	0	0	0.00
0.75	0	0.00	0.01	0.01	0.01	0.01	0.01	0.01	0	0	0	0	0	0	0	0	0.06
1.25	0.00	0.02	0.04	0.06	0.06	0.07	0.07	0.04	0.03	0.02	0.01	0.01	0.01	0.00	0.00	0.00	0.44
1.75	0	0.10	0.25	0.18	0.23	0.23	0.18	0.15	0.11	0.07	0.05	0.03	0.02	0.01	0	0.01	1.62
2.25	0	0.28	0.76	0.39	0.47	0.49	0.44	0.32	0.23	0.16	0.11	0.07	0.05	0.39	0	0	3.80
2.75	0	0	0	0.66	0.85	0.85	0.66	0.55	0.39	0.31	0.20	0.14	0.10	0	0	0	4.71
3.25	0	0	0	1.07	1.34	1.45	1.10	0.83	0.68	0.48	0.35	0.25	0.19	0.11	0	0	7.85
3.75	0	0	0	1.64	1.99	2.08	1.64	1.32	1.04	0.73	0.48	0.37	0.26	0.17	0.13	0	11.85
4.25	0	0	0	0	2.61	3.04	2.31	1.83	1.23	1.01	0.74	0.54	0.41	0.28	0	0	14.00
4.75	0	0	0	0	0	3.92	2.81	2.24	1.78	1.32	0.96	0.69	0.55	0.38	0	0	14.65
5.25	0	0	0	0	0	4.83	3.58	2.53	2.24	1.78	1.29	0.98	0.69	0	0.38	0	18.30
5.75	0	0	0	0	0	5.92	4.50	3.04	2.54	2.19	1.64	1.20	0.86	0	0.50	0.36	22.75
Sum	0.00	0.40	1.06	4.01	7.56	22.89	17.30	12.86	10.27	8.07	5.83	4.28	3.14	0.98	1.01	0.37	100.03

Table 8.6: Distribution (%) of weighted fatigue damage in most critical hotspot for worst cement level, head sea.

H_s/T_p	3.5	4.5	5.5	6.5	7.5	8.5	9.5	10.5	11.5	12.5	13.5	14.5	15.5	16.5	17.5	18.5	Sum
0.25	0	0	0	0	0	0.00	0	0	0	0	0	0	0	0	0	0	0.00
0.75	0	0.00	0.01	0.02	0.01	0.01	0.01	0.00	0	0	0	0	0	0	0	0	0.06
1.25	0.00	0.02	0.13	0.29	0.46	0.37	0.30	0.10	0.04	0.02	0.00	0.00	0.00	0.00	0.00	0.00	1.73
1.75	0	0.02	0.67	0.61	0.71	0.98	0.59	0.43	0.25	0.08	0.03	0.00	0.01	0.00	0	0.00	4.38
2.25	0	0.02	0.26	1.08	1.29	1.02	0.81	0.75	0.56	0.36	0.13	0.04	0.02	1.08	0	0	6.35
2.75	0	0	0	0.72	2.40	1.57	1.61	1.78	1.32	0.82	0.16	0.09	0.03	0	0	0	10.50
3.25	0	0	0	0.37	2.48	4.36	1.21	1.48	1.89	0.58	0.35	0.10	0.06	0.01	0	0	12.89
3.75	0	0	0	0.09	1.38	3.85	4.07	2.22	1.08	1.05	0.34	0.22	0.04	0.07	0.01	0	14.42
4.25	0	0	0	0	1.21	6.16	4.94	1.59	1.28	0.59	0.68	0.22	0.07	0.02	0	0	16.76
4.75	0	0	0	0	0	2.95	3.74	2.84	1.96	1.07	0.66	0.12	0.06	0.02	0	0	13.42
5.25	0	0	0	0	0	2.23	2.69	3.50	1.03	1.33	0.89	0.28	0.16	0	0.02	0	12.13
5.75	0	0	0	0	0	1.03	1.30	1.76	0.88	0.89	0.57	0.62	0.25	0	0.03	0.02	7.35
Sum	0.00	0.06	1.07	3.18	9.94	24.53	21.27	16.45	10.29	6.79	3.81	1.69	0.70	0.13	0.06	0.02	99.99

It is worth noting the great influence the significant wave height has on estimated fatigue. The weighted fatigue damage distribution in Table 8.6 shows that the sea states with $H_s \geq 2.75$ m, which accounts for 44 % of the total time of the operation, contributes to over 87 % of the estimated fatigue damage. Considering a relatively low cut-off limit could therefore result in a significant increase in fatigue life, however, this would also increase the total operation time, which may not be acceptable.

The estimated fatigue damage without template support for static and cyclic p-y curves, normalized with respect to the former, is listed for all hotspots in Table 8.7. The effect from the cyclic curves is negligible, as the reduction in estimated fatigue damage is 0.04 - 0.5 %. This shows that greater conductor displacements are needed to get a noticeable effect from using cyclic p-y curves. It is however uncertain if displacements of this order is realistic.

Table 8.7: Total fatigue damage normalized with respect to static p-y curves, worst cement level, no template support.

	Static	Cyclic
Hotspot 1	1.0000	0.9994
Hotspot 2	1.0000	0.9996
Hotspot 3	1.0000	0.9994
Hotspot 4	1.0000	0.9961
Hotspot 5	1.0000	0.9951

The fatigue damage development for the four different cases, i.e. base case, diffracted kinematics, soil damping and reduced drag, is shown for the most critical hotspot in Figure 8.12 and 8.13. The total estimated fatigue damage, normalized with respect to the base case, is listed for head sea and beam sea in Table 8.8 and 8.9, respectively.

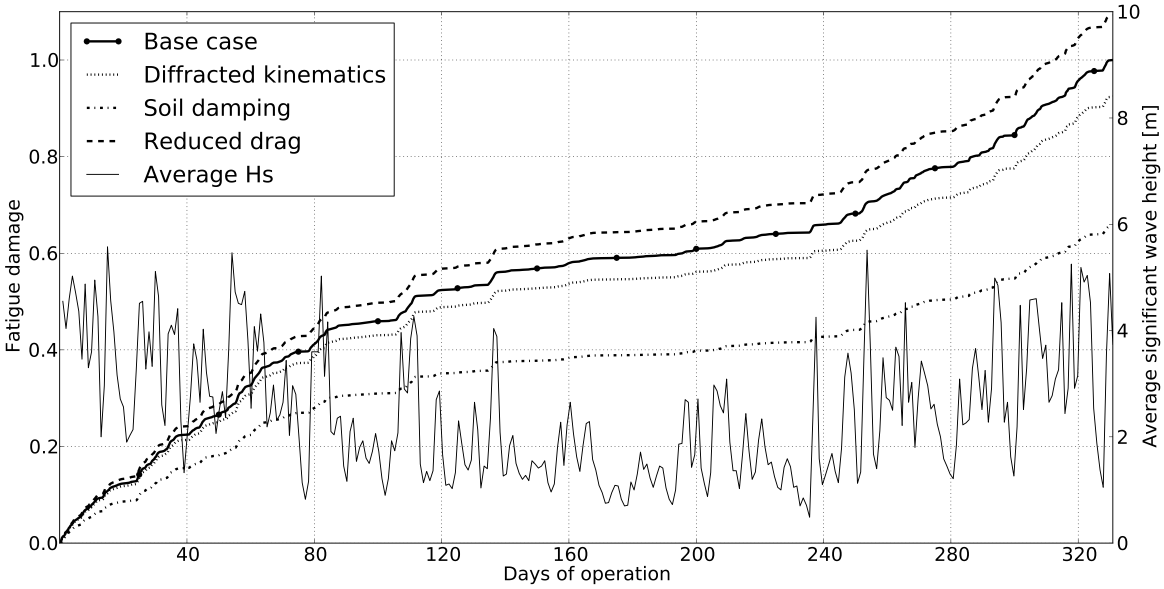

Figure 8.12: Normalized fatigue damage development in most critical hotspot for worst cement level, head sea.

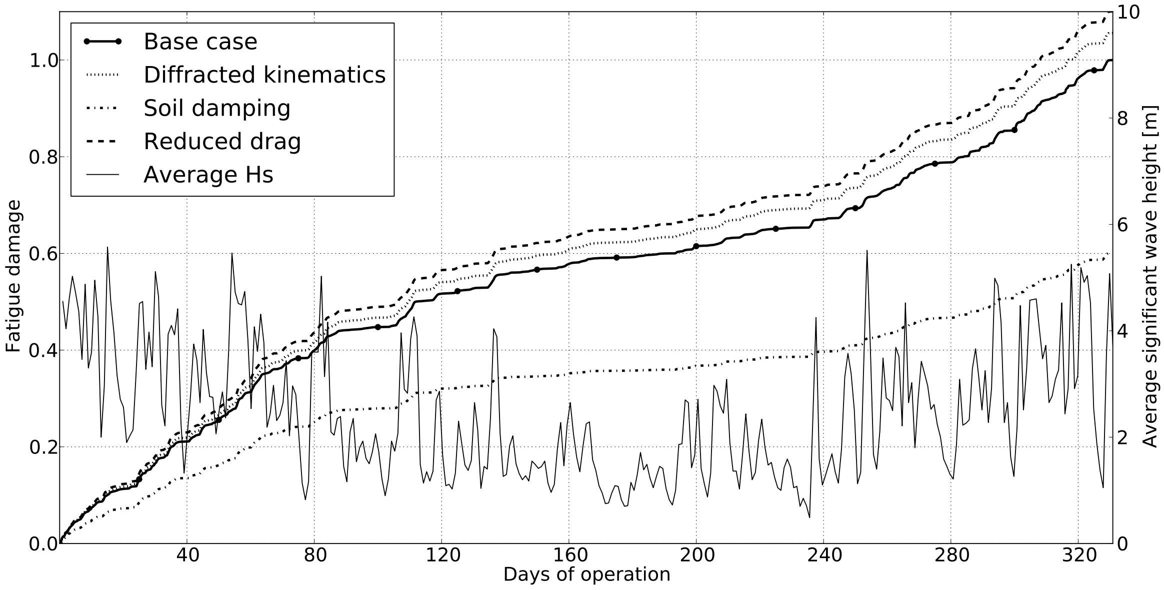

Figure 8.13: Normalized fatigue damage development in most critical hotspot for worst cement level, beam sea.

Table 8.8: Total fatigue damage normalized with respect to the base case, head sea.

	Damage
Base case	1.00
Diffracted kinematics	0.92
Soil damping	0.66
Reduced drag	1.09

Table 8.9: Total fatigue damage normalized with respect to the base case, beam sea.

Case	Damage
Base case	1.00
Diffracted kinematics	1.06
Soil damping	0.60
Reduced drag	1.10

As the figures and tables show, neither the effect of diffracted kinematics nor reduced drag are significant. A 23.5 % decrease in the drag force increases the estimated fatigue damage with approximately 10 % for both wave headings. Diffraction effects from the MODU reduce the estimated damage in head sea with 8 %, while the estimated damage in beam sea waves is increased by 6 %. Considering the great uncertainties in a wellhead fatigue analysis, the effect from these modifications is relatively small. Introducing soil damping however, is seen to have a large impact on the results, as the estimated fatigue damage is reduced with 34-40 %. The effect is greatest for the sea states with small spectral peak periods, as seen in Table 8.10, where the estimated damage is reduced with up to 90 %. This is expected, since the viscous damping force is proportional to the velocity, and low values of T_p means a relatively high oscillating frequency. However, the method used to include soil damping in the analysis is not ideal, and there are great uncertainties associated with the results. This is further discussed in Section 8.4.

Table 8.10: Damage per hour sea state with soil damping relative to base case, most critical hotspot for worst cement level, head sea.

H_s/T_p	3.5	4.5	5.5	6.5	7.5	8.5	9.5	10.5	11.5	12.5	13.5	14.5	15.5	16.5	17.5	18.5
0.25	0	0	0	0	0	0.59	0	0	0	0	0	0	0	0	0	0
0.75	0	0.09	0.11	0.25	0.40	0.49	0.53	0.55	0	0	0	0	0	0	0	0
1.25	0.14	0.11	0.13	0.26	0.45	0.53	0.59	0.55	0.60	0.56	0.59	0.53	0.55	0.56	0.60	0.55
1.75	0	0.14	0.14	0.32	0.44	0.54	0.58	0.61	0.62	0.61	0.59	0.60	0.58	0.58	0	0.58
2.25	0	0.14	0.14	0.37	0.49	0.55	0.59	0.61	0.63	0.61	0.62	0.62	0.61	0.37	0	0
2.75	0	0	0	0.42	0.56	0.60	0.61	0.65	0.64	0.64	0.61	0.62	0.63	0	0	0
3.25	0	0	0	0.47	0.60	0.63	0.65	0.64	0.66	0.68	0.64	0.64	0.64	0.62	0	0
3.75	0	0	0	0.51	0.64	0.69	0.66	0.66	0.69	0.67	0.66	0.65	0.64	0.63	0.64	0
4.25	0	0	0	0	0.66	0.71	0.70	0.69	0.67	0.69	0.68	0.66	0.65	0.66	0	0
4.75	0	0	0	0	0	0.75	0.72	0.70	0.70	0.71	0.68	0.69	0.67	0.65	0	0
5.25	0	0	0	0	0	0.75	0.75	0.72	0.72	0.72	0.70	0.70	0.67	0	0.68	0
5.75	0	0	0	0	0	0.76	0.77	0.71	0.71	0.72	0.71	0.70	0.69	0	0.71	0.70

The effect of wave directionality is shown in Figure 8.14, and the total normalized damage for the six analysed points can be found in Table 8.11. It is emphasized that only one wave heading is used in the global analysis, and that the wave directions are only taken into account in the fatigue assessment. The results are therefore only valid for RAOs independent from wave heading, which is not the case. However, the reduction in estimated fatigue damage of approximately 25 % for both head sea and beam sea indicates that a significant improvement in fatigue life can be expected for all wave headings in the applied environmental conditions.

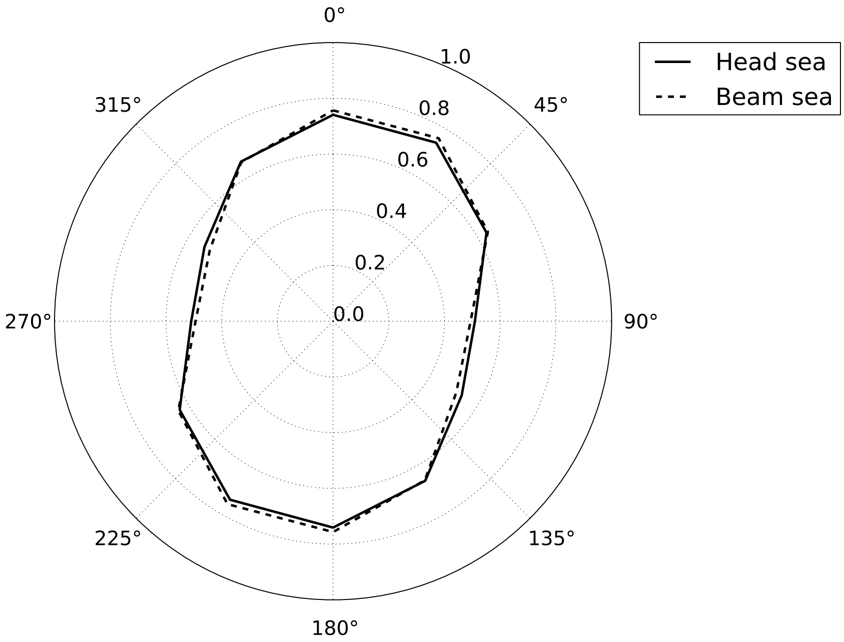

Figure 8.14: Normalized fatigue damage distributed around circumference in most critical hotspot for worst cement level.

Table 8.11: Total fatigue damage distributed around circumference normalized with respect to base case, most critical hotspot, worst cement level.

Circumference point	Angle (relative to true north)	Damage (head sea)	Damage (beam sea)
1	270°	0.51	0.49
2	300°	0.53	0.51
3	330°	0.66	0.66
4	0°	0.74	0.76
5	30°	0.74	0.76
6	60°	0.64	0.64

8.4 Uncertainties and Assumptions

A wellhead fatigue analysis contains a great number of assumptions and simplifications, contributing to uncertainty regarding the results. Some of the most important uncertainties and assumptions in the current method are summarized in this section.

8.4.1 p-y Curves

The method used to represent soil stiffness in the analysis, i.e. the p-y method, was initially developed in the 1970s for offshore jacket platforms, using a quasi-static approach. This means that nonlinear stiffness behaviour originating from stress history and load frequency is not considered, which may have significant consequences for the accuracy of the model, as the soil can experience great changes in stiffness due to these effects (van Buren and Muskulus, 2012). Additionally, soil damping, shown in the results to have a large impact on estimated fatigue life, is not included in the method.

8.4.2 SN Curves

The design SN curve used in the fatigue damage assessment is found from the mean curve minus two standard deviations for relevant experimental data, which in most cases will lead to conservative fatigue damage estimates. The experimental SN curves are found from loading with constant amplitude, and a Haibach model is applied to account for the variable amplitude loading. The Haibach model is more conservative and accurate than a model where cycles below the fatigue limit is non-damaging (Berge, 2006), but there is still some uncertainty associated with the accuracy of the model.

8.4.3 Miner-Palmgren Summation

The fatigue damage assessment is carried out using the Miner-Palmgren summation procedure, where the damage per load cycle is assumed to be constant at a given stress range. A shortcoming with the procedure is that it does not take the order of the loading into account, and therefore assumes that the mechanisms of damage is unchanged throughout the structure's lifetime. The hypothesis is also known to frequently overestimate fatigue life (Miller et al., 1986).

8.4.4 Cement Level

Cement shortfall is shown to have a significant effect on estimated fatigue life, and it is almost impossible to confirm cement level information on a specific well (DNV, 2011a). A worst case cement level is therefore often assumed, leading to conservative fatigue life estimates.

8.4.5 Vessel RAO

The RAOs for the MODU used in the analysis are of the first order. This means that higher order effects, which can influence the wellhead bending moment, are not included.

8.4.6 Environmental Conditions

When estimating the fatigue life of a wellhead for a future operation, a wave scatter diagram from the drilling location is used. The scatter diagrams are based on historical observations, and variations in the weather from one year to another will therefore introduce uncertainty. In addition, wave spreading is not taken into account in the analysis, which will result in conservative fatigue life estimates as all wave loading will be applied in one plane. Holm et al. (2013) showed that the effect of introducing weather directionality and wave spreading significantly improved the fatigue life, which is also indicated in the previous section of this thesis. It can, however, be difficult to justify non-conservative directional assumptions for future operations.

8.4.7 Damping

Damping from soil and the riser itself is usually not included in the analysis. In addition, current, which contributes to damping of the system, is assumed to have a conservatively low velocity. In this thesis, soil damping is shown to have a great impact on estimated fatigue damage, and Holm et al. (2013) showed that applying structural damping in the riser and the LFJ has a similar effect. However, several simplifications have been made in order to be able to include soil damping in the analysis. Material soil damping is found to be dependent on both oscillating frequency and amplitude, while a constant damping coefficient is applied in Sima/Riflex. In addition, a shear stress-strain curve had to be assumed for the soil, as no data from location was available. While there is a high degree of uncertainty associated with the applied damping coefficients, the effect of damping is shown to be important, and should be a subject for future studies.

8.4.8 Modelling of Lower Stack

In the global analysis, the lower stack is modelled using beam elements with constant stiffness, and the hydrodynamic coefficients are found assuming a rectangular cross-section. In reality, the BOP and the LMRP have varying properties with length. Correct modelling of the lower stack can affect the results, however, Harildstad and Haukanes (2013) showed that using BOP stiffness found from a detailed 3D FE model in the analysis had a negligible effect on estimated fatigue life.

8.4.9 Drag Coefficient

A constant drag coefficient $C_D = 1.0$ is used for the riser in all analyses. However, the drag coefficient for a circular cylinder is shown to be highly dependent on the Keulegan-Carpenter (KC) number, see e.g. Sarpkaya (1976) or Chakrabarti (1987), which suggests that the drag coefficient will vary along the length of the riser. There is, however, uncertainties connected to the applicability of the results, as the coefficients are found from laboratory tests, where effects from real life operations are not taken into account.

8.4.10 Vortex-Induced Vibrations

Vortex-induced vibrations (VIV) are caused by vortices that are shed on both sides of the riser in a cyclic manner under current loads. VIV may contribute to wellhead fatigue damage, and it has been confirmed to occur in deepwater drilling risers (Tognarelli et al., 2010). Guidance on how to include effects from VIV are not included in the current analysis method, but is planned to be included in the final version of the document (DNV, 2011a).

9 Conclusions

The current analytical wellhead fatigue analysis method has been shown to be overly conservative compared to full scale measurements (Russo et al., 2012). The objective of the thesis was to identify uncertainties in the method, and to suggest improvements where the current modelling was found to be insufficient. A fatigue assessment of a typical wellhead system has been performed, where the fatigue damage has been estimated in five hotspots for a one year long historical operation.

Using cyclic p-y curves had no effect on estimated wellhead fatigue for the original wellhead system, as the displacements along the conductor was smaller than the critical value for all force increments. If the template support was removed, an effect was seen for large bending moments, however, the impact on estimated fatigue was negligible. For the p-y method used in the analysis, significantly larger conductor displacements are required to get a noticeable effect from cyclic curves, which may not be realistic.

A smaller hydrodynamic diameter, found from the projected diameter for a flow direction perpendicular to the one giving maximum drag, was shown to increase the fatigue damage slightly. Diffraction effects from the MODU resulted in a small reduction in wellhead bending moment for low wave periods in head sea waves, but caused a slight increase in wellhead bending moment for all wave periods in beam sea. The effect on fatigue life for these modifications was small, as the change in estimated fatigue damage for the operation was less than 10 % in both cases. Soil damping was shown to have a great effect on the estimated fatigue damage, especially in sea states with small T_p, and resulted in significantly improved fatigue life. However, the methodology used to implement damping was based on several simplifications and assumptions. In order to secure accurate results, the damping values need to be quantified.

Variation of the main wave direction, which distributes the fatigue damage around the circumference of the hotspot, was also found to improve the fatigue life. The results are only valid for RAOs which are identical in all directions, something which is not the case. However, the results found from head sea and beam sea suggests that a significant increase in fatigue life can be obtained if weather directionality is accounted for, which was also the conclusion made by Holm et al. (2013). In addition, using the most unfavourable wave direction for all analyses will contribute to conservative fatigue life estimates, as the total fatigue damage from the operation was found to be several times higher for one wave heading than another.

10 Recommendations for Further Work

The most important result from the analysis is the significant effect from soil damping on estimated wellhead fatigue. It is therefore recommended that future studies focuses on development of more reliable and accurate implementations of soil damping, as the methodology used in this thesis is based on several simplifications and therefore is associated with a high degree of uncertainty. This would require detailed soil data from the drilling location and should, if possible, be verified against measurements.

It is also suggested that the possibility for a more accurate method of modelling soil-structure interaction is studied, as the p-y method used in the analysis has several shortcomings with regards to representation of dynamic systems. An alternative method including soil damping and nonlinear dynamic stiffness effects has been discussed for bottom-fixed offshore wind turbines, see van Buren and Muskulus (2012), however, no implementation of the method for subsea drilling has been found in the literature.

Russo et al. (2012) have shown that the analytical wellhead fatigue analysis method is conservative compared to a method using measured riser loads, which indicates that the global analysis overestimates the bending moments on the wellhead. A suggestion for further work would therefore be full scale measurements of strain at different locations on the conductor, in order to investigate the accuracy of the local FE model. The results could be used to modify the local model if deemed necessary, which would affect the load-to-stress curves and therefore also the estimated wellhead fatigue damage.

The reduction in drag force from a smaller hydrodynamic diameter was shown to have relatively little effect on estimated fatigue damage. There are, however, great uncertainties associated with the drag coefficient, as the values for C_D usually are found from laboratory tests, and are also seen to vary with the KC number and the surface roughness. A more detailed study on the drag coefficient could therefore contribute to reduce the uncertainty in the global riser analysis.

References

Almar-Næss, A., Andersson, H., Bardal, E., Berge, S., Engesvik, K., Fines, S., Gibstein, M., Haagensen, P. J., Karlsen, A., Lereim, J., Lotsberg, I., Moan, T., Moe, E. T., Slatcher, S. and Wästberg, S. (1985), *Fatigue Handbook - Offshore Steel Structures*, Tapir.

Anzai, H. and Endo, T. (1979), 'On-site indication of fatigue damage under complex loading', *International Journal of Fatigue* **1**(1), 49–57.

API (2011), 'API RP 2GEO Geotechnical and Foundation Design Considerations'.

ASTM (2011), 'E1049-85 Standard Practices for Cycle Counting in Fatigue Analysis'.

Berge, S. (2006), 'Fatigue and fracture design of marine structures II: Fatigue design of welded structures'. Department of Marine Technology, NTNU.

Brodtkorb, P., Johannesson, P., Lindgren, G., Rychlik, I., Rydén, J. and Sjö, E. (2000), WAFO - a Matlab toolbox for the analysis of random waves and loads, *in* 'Proceedings of the 10th Internatonal Offshore and Polar Engineering Conference', Vol. 3, pp. 343–350.

Chakrabarti, S. K. (1987), *Hydrodynamics of Offshore Structures*, Computational Mechanics Publications.

Cook, R. D., Malkus, D. S., Plesha, M. E. and Witt, R. J. (2002), *Concepts and Applications of Finite Element Analysis*, John Wiley & Sons.

DNV (2010), 'DNV-OS-F201 Dynamic risers'.

DNV (2011a), 'Wellhead fatigue analysis method'. 2011-0063/ 12Q5071-26 Rev 01.

DNV (2011b), 'DNV-OS-C101 Design of offshore steel structures, general (LRFD method)'.

DNV (2012a), 'DNV-RP-C203 Fatigue design of offshore steel structures'.

DNV (2012b), 'DNV-RP-H103 Modelling and analysis of marine operations'.

DNV (2013), 'Sesam user manual - Wadam'.

Eiksund, G. R. (2014), 'Personal communication'.

Faltinsen, O. M. (1990), *Sea Loads on Ships and Offshore Structures*, Cambridge University Press.

Gazetas, G. and Dobry, R. (1984), 'Horizontal response of piles in layered soils', *Journal of Geotechnical Engineering* **110**(1), 20–40.

Grytøyr, G. and Steinkjer, O. (2012), Uncertainty of long term fatigue load of subsea well heads, *in* 'Proceedings of the 31st International Conference on Ocean, Offshore and Arctic Engineering', Vol. 6, pp. 639–646.

Harildstad, E. and Haukanes, A. (2013), Effects of BOP stack modelling on estimated wellhead fatigue damage, Master's thesis, Norwegian University of Science and Technology (NTNU).

Hasselmann, K., Barnett, T. P., Bouws, E., Carlson, H., Cartwright, D. E., Eake, K., Euring, J. A., Gicnapp, A., Hasselmann, D. E., Kruseman, P., Meerburg, A., Mullen, P., Olbers, D. J., Richren, K., Sell, W. and Walden, H. (1973), 'Measurement of wind wave growth and swell decay during the Joint North Sea Wave Project (JONSWAP)', *Deutschen Hydrographischen Zeitschrift Reihe A* **8**(12).

Holm, H. G., Holden, H. and Russo, M. (2013), Wellhead fatigue analysis method: Steps for improving the quality of the global riser analyses, *in* 'Proceedings of the 23rd International Offshore and Polar Engineering Conference', pp. 161–169.

ISO (2009), '13624-1 Design and operation of marine drilling riser equipment'.

ISO (2010), '13624-2 Deepwater drilling riser methodologies, operations, and integrity technical report'.

Kagawa, T. (1992), 'Moduli and damping factors of soft marine clays', *Journal of Geotechnical Engineering* **118**(9), 1360–1375.

Langen, I. and Sigbjörnsson, R. (1979), *Dynamisk Analyse av Konstruksjoner*, Tapir.

Larsen, C. M. (1990), 'Response modelling of marine risers and pipelines'. NTNU, division of Marine Structures.

Larsen, C. M. (2008), 'Aspects of marine riser analysis'. NTNU, Department of Marine Structures.

Larsen, C. M. (2013), 'Personal communication'.

Mansour, A. and Liu, D. (2008), *Strength of Ships and Ocean Structures*, The Society of Naval Architects and Marine Engineers.

MARINTEK (2013*a*), 'Riflex theory manual'. Sintef.

MARINTEK (2013*b*), 'Riflex user's manual'. Sintef.

Mather, A. (1995), *Offshore Engineering: An Introduction*, Witherby & Co Ltd.

Matlock, H. (1970), Correlations for design of laterally loaded piles in soft clay, *in* 'Proceedings of the 2nd Annual Offshore Technology Conference', pp. 577–594.

Miller, K. J., Mohamed, H. J. and de los Rios, E. R. (1986), 'Fatigue damage accumulation above and below the fatigue limit', *The Behaviour of Short Fatigue Cracks* pp. 491–511. Mechanical Engineering Publications, London.

Mosalam, K. M. (2013), ‘CE222 - Finite Element Methods’. University of California, Berkeley.

Næss, A. and Moan, T. (2013), *Stochastic Dynamics of Marine Structures*, Cambridge University Press.

Ray, R. P. and Woods, R. D. (1988), ‘Modulus and damping due to uniform and variable cyclic loading’, *Journal of Geotechnical Engineering* **114**(8), 861–876.

Reinås, L., Russo, M. and Grytøyr, G. (2012), Wellhead fatigue analysis method: The effect of variation of lower boundary conditions in global riser load analysis, *in* ‘Proceedings of the 31st International Conference on Ocean, Offshore and Arctic Engineering’, Vol. 1, pp. 283–295.

Russo, M., Holden, H., Reinås, L. and Sæther, M. (2012), Fatigue assessment of subsea wells for future and historical operations based on measured riser loads, *in* ‘Proceedings of the 31st International Conference on Ocean, Offshore and Arctic Engineering’, Vol. 1, pp. 139–150.

Sarpkaya, T. (1976), Vortex shedding and resistance in harmonic flow about smooth and rough circular cylinders at high Reynolds numbers, Technical Report NPS-59SL76021, Naval Postgraduate School, Monterey, CA.

Sheffield, R. (1980), *Floating Drilling: Equipment and Its Use*, Gulf Publishing Company.

Sparks, C. P. (1984), ‘The influence of tension, pressure and weight on pipe and riser deformations and stresses’, *Journal of Energy Resources Technology* **106**(1), 46–54.

Stange, I. (2012), Comparison between measured and calculated riser response, Master’s thesis, Norwegian University of Science and Technology (NTNU).

Tognarelli, M. A., Campbell, M. and Deka, D. (2010), Drilling riser VIV - fact or fiction?, *in* ‘IADC/SPE Drilling Conference and Exhibition’, Vol. 2, pp. 1272–1282.

van Buren, E. and Muskulus, M. (2012), ‘Improving pile foundation models for use in bottom-fixed offshore wind turbine applications’, *Energy Procedia* **24**, 363–370.

Appendix A

Transfer Curves

A.1 Hotspot 1

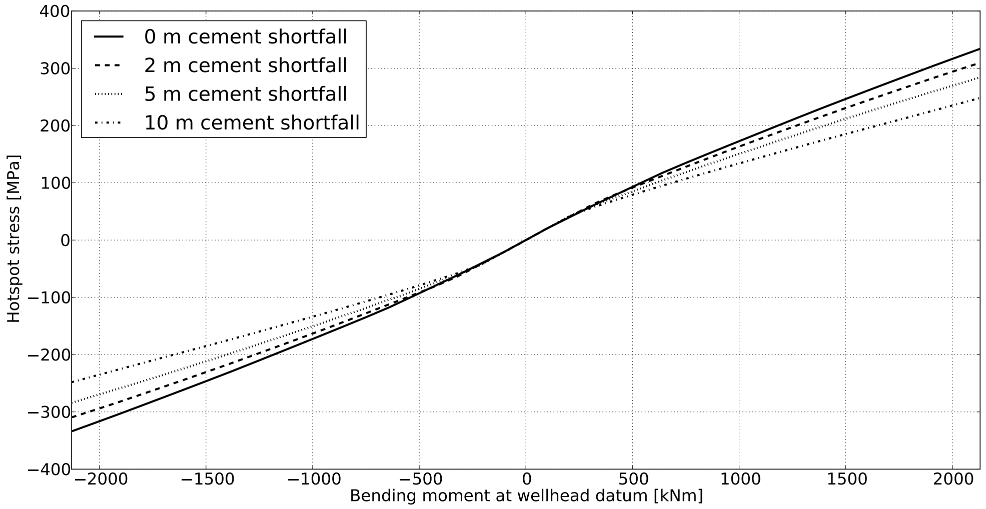

Figure A.1: Load-to-stress curve for hotspot 1.

A.2 Hotspot 2

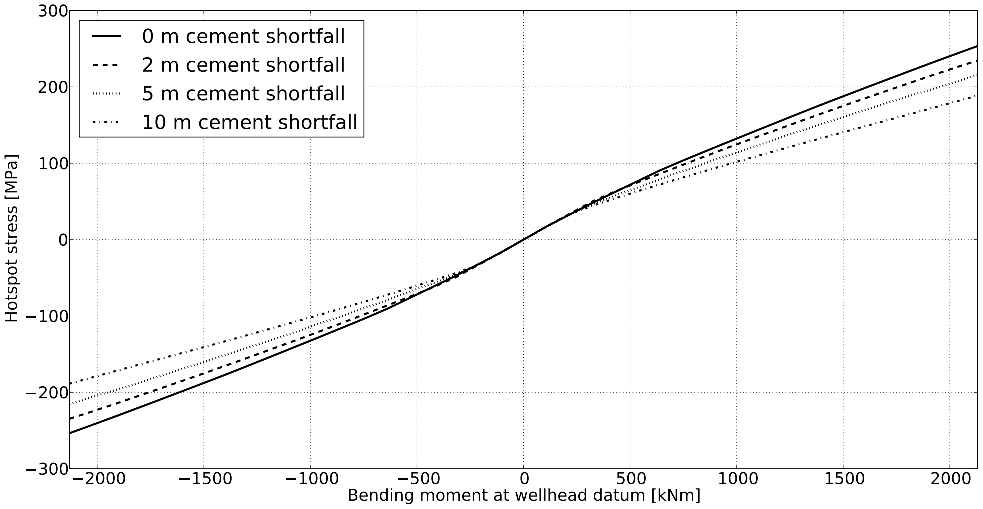

Figure A.2: Load-to-stress curve for hotspot 2.

A.3 Hotspot 3

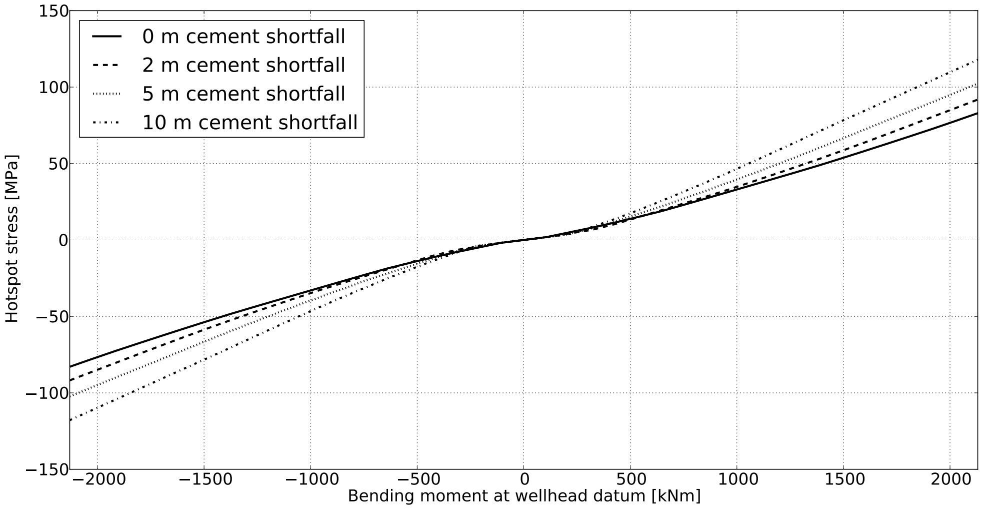

Figure A.3: Load-to-stress curve for hotspot 3.

A.4 Hotspot 4

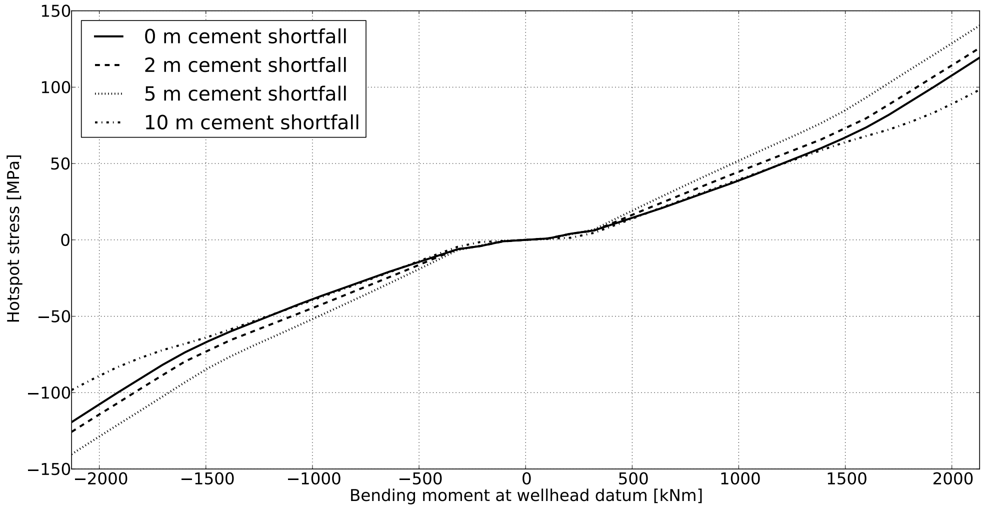

Figure A.4: Load-to-stress curve for hotspot 4.

A.5 Hotspot 5

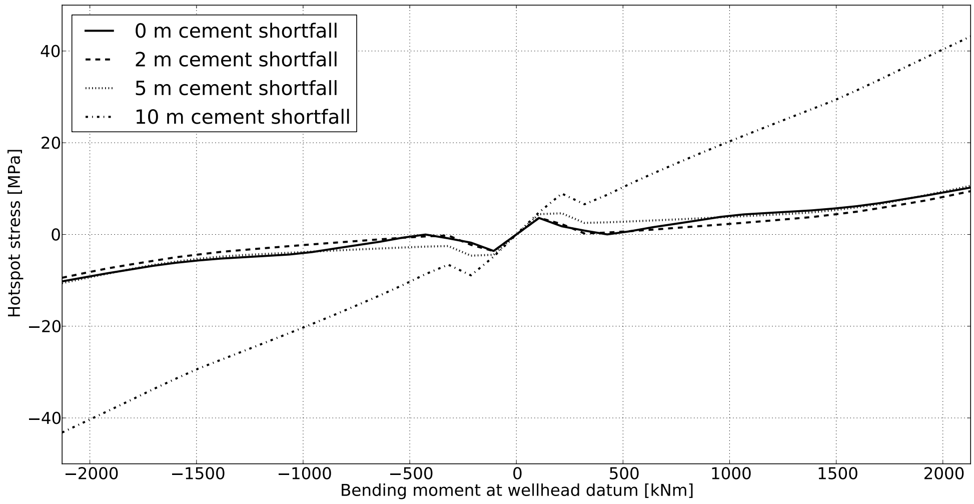

Figure A.5: Load-to-stress curve for hotspot 5.

Appendix B

Scripts

The scripting language Python was used for most of the pre- and post-processing in the project. Important scripts are included on an attached memory stick, and an overview of the files and their functions are presented in the following sections.

B.1 localanalysis.py

The purpose of localanalysis.py is to create the local model in Abaqus as described in DNV (2011a), based on wellhead system coordinates and p-y curves from input files. Cement shortfall, and location of solid-beam transition and model termination, are chosen by the user.

B.2 displacements.py

The purpose of displacements.py is to read the displacements along the conductor for each load increment in Abaqus, and write them to file.

B.3 damping.py

The purpose of damping.py is to use conductor displacements from file to estimate material soil damping using a Ramberg-Osgood model and the method described in Gazetas and Dobry (1984). The R-O model parameters and soil properties are defined by the user.

B.4 damage.py

The purpose of damage.py is to calculate the fatigue damage for all cases, headings, cement levels and hotspots, both for the whole operation and for each individual sea state. The script imports stress ranges found from rainflow counting using the WAFO package in Matlab, and uses SN curves and Miner-Palmgren summation to find the fatigue damage.